energies

MDPI

Article

A Coupled Model of Two-Phase Fluid Flow and Heat Transfer to Transient Temperature Distribution and Seepage Characteristics for Water-Flooding Production Well with Multiple Pay Zones

Guoshu Huang [1], Huolin Ma [1,*], Xiangyun Hu [1,*], Jianchao Cai [1], Jiabin Li [2], Hongqing Luo [1] and Heping Pan [1]

1 Hubei Subsurface Multi-scale Imaging Key Lab, Institute of Geophysics & Geomatics, China University of Geosciences, Hubei, Wuhan 430074, China; hgsgeoman@163.com (G.H.); caijc@cug.edu.cn (J.C.); lhqcug@163.com (H.L.); panpinge@163.com (H.P.)

2 Institute of Geological Survey of Guizhou, Geological & Geophysical Development Application Engineering Technology Research Center, Guizhou, Guiyang 550081, China; 061041@163.com

* Correspondence: mhl70@163.com (H.M.); xyhu@cug.edu.cn (X.H.); Tel.: +86-189-0864-8929 (H.M.); +86-139-9565-0995 (X.H.)

Received: 10 April 2019; Accepted: 13 May 2019; Published: 15 May 2019



Abstract: Temperature is one of the most prominent factors affecting production operations, predicting the accurate wellbore-formation temperature in a water-flooding production well is of great importance for multiple applications. In this paper, an improved coupled model of oil–water two-phase fluid flow and heat transfer was developed to investigate the transient temperature behavior for a producing well with multiple pay zones. Firstly, a novel method was derived to simulate the water saturation and the water breakthrough time (WBT) for tubing, which are key monitoring parameters in the process of water flooding. Then, we incorporated water saturation and an equation set for immiscible displacement to calculate the seepage velocity and the pressure of the two-phase fluid in the pay zones. Next, the upward seepage velocity of the tubing fluid change with depth was focused on, and the proper coupled initial and boundary conditions are presented at the interfaces, therewith the implicit finite difference method was used to compute the transient temperature with the input of the seepage characteristics for the reservoirs. Meanwhile, the validity of the proposed model has been verified by the typical model. Finally, a sensitivity analysis delineated that the production rate and the production time had a significant impact on the tubing fluid temperature. The overburden was hotter with a lower volumetric heat capacity or a higher thermal conductivity. In addition, the sensitivity of the porosity and the irreducible water saturation to formation temperature was significantly different before and after the WBT. The coupled model presented herein helps to advance the transient seepage characteristics analysis of pay zones, the precise temperature prediction is very useful for reservoir characterization and production analysis purposes and provides insight for designing the exploitation scheme in deep reservoirs and geothermal resources.

Keywords: transient coupled heat transfer model; water flooding; two-phase flow; seepage characteristics; wellbore-formation; multiple pay zones

1. Introduction

Knowing the precise wellbore-formation temperature in various kinds of producing wells is a serious challenge of great importance for multiple applications in deep reservoirs and geothermal resource exploration and exploitation. The temperature is one of the most prominent factors affecting

production operations, including reservoir characterization and the qualitative or quantitative interpretation of fluid rheology, cementing quality, thermal fatigue failure, pressure control and stability for wellbore, etc. [1–3].

In the past few decades, simulation technology of fluid flow and heat transfer processes has been an essential vehicle for scientific research and applications [4]. Many scholars have studied the downhole temperature distribution of various kinds of production wells because it can effectively reflect production or injection history, especially for interpreting problem wells or extracting abundant information [5]. Despite the many efforts that have been made on developing accurate multiphase flow and heat transfer over the last decades, the complex nature of this issue still motivates several studies [6].

One of the earliest works on predicting the temperature distribution in a hydrocarbon exploited well was presented by Lauwerier et al. [7] and Lesem et al. [8], who took into account the long-time water-injection operation with the ultimate goal of improving oil recovery. Subsequently, significant advances have occurred in downhole temperature prediction since the seminal work of Ramey [9], whose landmark work addressed approximate methods to simulate the temperature of single-phase incompressible liquid and ideal gas flowing in injection or production wells. Satter [10] proposed a method to improve Ramey's model [9] by incorporating the phase change effects for steam injection wells. Raymond [11] developed one of the first fully transient models for wellbore heat transfer. Afterwards, Raymond's method [11] was improved by Marshall and Bensten [12] with an advanced algorithm for the solution of the governing equations in a discretized form. In the 1990s, Hasan and his coworkers presented a few wellbore/reservoir temperature models for gas, oil and two-phase flows [13–15], the wellbore models were coupled with the analytic reservoir models, their formulas of finite-difference form were derived from coupled mass, momentum, and energy equations; hence the time-consuming separate matrix operations were required. Therewith, Izgec et al. [16] presented the transient wellbore model coupled with a semi-analytic temperature solution, which computed the fluid temperature profile in flowing and shut-in wells. Wu et al. [17] derived a pseudo-3D model to compute the downhole heat transfer during the fluid circulation in the annulus. In addition, intelligent algorithms can also be used to calculate the temperature of the producing well, Farshad et al. [18] constructed two kinds of artificial neural network (ANN) models, which can simulate the flowing fluid temperature of the oil well at any depth. Lee et al. [19] presented a method to predict the formation temperature and thermal properties from the borehole data based on a genetic algorithm (GA).

However, there are few works in the above studies relating temperature profile estimation with the reservoir fluid flow. One of the basic works was presented by Romero-Juarez [20], which was modified by Curtis and Witterholt [21], this model can determine the relationship between the fluid temperature and flow rate of each zone. Smith and Steffens [22] studied how some factors (the water leakoff, reservoir temperature, et al.) affect the temperature profiles in water injection wells. Ganguly [23] derived a model of accounting for the heat transport processes for advection, which predicts the transient temperature distribution and thermal-front movement in a heterogeneous porous confined geothermal reservoir. Nevertheless, their model can only be applied to a single-phase flow. Hence a new attempt was made by Shi et al. [24], who proposed an improved numerical method to simulate the downhole temperature distribution for producing oil wells with multiple pay zones, the heat convection was highly regarded due to the fluid flow from the porous formation to the wellbore, but the fluid velocity and the saturation variation of oil–water two-phase pay zones that change with production times were ignored. Subsequently, Mostofinia et al. [25] presented a novel coupled model to calculate the temperature and pressure distribution of production wells with multiple pay zones as multiphase fluid flow from a nonhomogeneous reservoir, and the oil degassing was also accounted for in this model to increase the accuracy of the method. Shang and Sarica [26] conducted a mathematical model to evaluate tubing fluid temperature profiles of oil–water two-phase stratified flows in an offshore deep-water producing environment. More recently, Hasan and Kabir [27] developed a unified method to present the heat behavior during production, and the model is applicable for both single-flow and multiple-flow conduits under the steady-state or unsteady-state conditions. Mao and

Zeidouni [28] proposed a temperature transient analysis solution for a bounded oil reservoir under radial boundary dominated flow, which can be integrated with previous transient temperature to simulate the temperature signal from a depletion drive production well.

For decades, although great successes had been achieved, and many analytical and numerical approaches have been used to simulate the downhole temperature distribution under steady and unsteady-heat-flow conditions, many simulations have been widely applied in industrial practices, in most of the mentioned studies, the impacts of the complex wellbore configuration and the multiple adjacent formations (multiple pay zones) are usually ignored, and the thermal interaction between the flow and the environment were not highly regarded, especially the effects of the fluid seepage of the pay zones on the temperature field. Thus there is little relevant research on the downhole transient temperature distribution for water-flooding production well of multiple pay zones.

The present work develops a coupled model to study the transient temperature distribution and the seepage characteristics for a water-flooding production well. To better describe the temperature behavior, the non-piston-like displacement (plane radial flow) of pay zones and the upward seepage velocity of the tubing fluid that changes with depth were accounted when the reservoir and wellbore models were coupled. We first derived a novel method to simulate the water saturation and the water breakthrough time (WBT). Then we incorporated water saturation and an equation set for immiscible displacement to calculate the other seepage parameters (including the seepage velocity and the pressure etc.) of the pay zones. Next, the coupled temperature model was formulated for the reservoir domain and the wellbore domain based on the principles of mass, momentum, and energy conservation. Therewith the implicit finite difference method was used to compute the transient temperature field with the input of the seepage characteristics for the reservoir fluid. Further, a typical model is provided to illustrate the feasibility of the proposed model. Finally, a sensitivity analysis was carried out to provide valuable knowledge of production optimization in terms of production factors, reservoir properties and geological conditions, etc. which is helpful to analyze effects from different parameters for the temperature distribution.

2. Modeling Approach

2.1. Coupled Mathematic Model of Fluid Flow and Heat Transfer

2.1.1. Fluid Flow and Heat Transfer Model in Pay Zones

Based on the Buckley-Leverett (BL) displacement theory, in the process of water drive production, the gravitation effect and the capillary pressure can be ignored for the flat formation scale, thus the water drive process of the reservoir was considered as 1-D plane-radial flow (non-piston-like displacement) in this model [29]. The reservoir can be divided into three parts between the supply edge and the tubing: water zone; oil–water mixed zone; oil zone. In addition, as the production time goes on, the mixed zone of the oil–water two-phase fluid gradually expands to the tubing, Figure 1 shows this process. Therefore the seepage velocity and saturation of two-phase fluid would change with production time and radial position in the pay zones. In addition, the fluid seepage velocity is closely related to thermal convection, at the same time, the fluid saturation variation will affect the equivalent thermophysical properties of the pay zones.

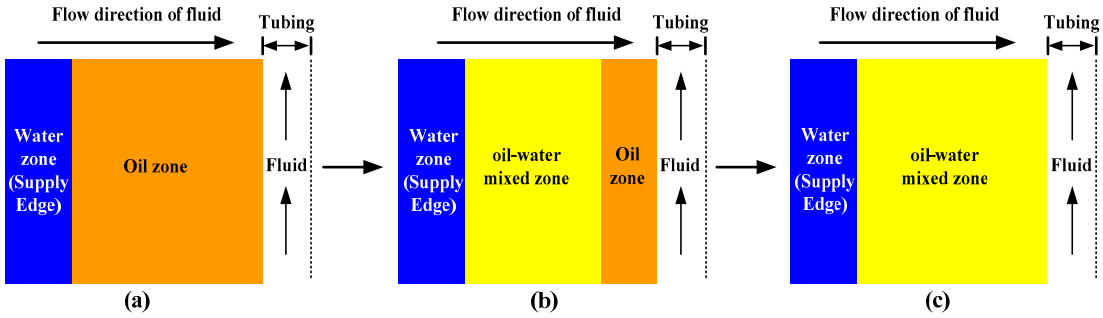


Figure 1. Schematic illustration of the water displacing oil process for 1-D plane-radial flow: (**a**) the initial state ($t = 0$); (**b**) before the water breakthrough time for tubing ($t < t_w$); **(c)** after the water breakthrough time for tubing ($t \geq t_w$).

2.1.2. Fluid Flow and Heat Transfer Model in Tubing

After the fluids in the upper pay zones enter the tubing, they would mix with the fluids from the lower pay zones (the fluids in the lower pay zones are hotter than the fluids in the upper pay zones), which would cause their temperature to be higher than the adjacent formation [30]. Due to such temperature difference, heat can be transferred to the formations from the tubing fluid by the way of conduction and convection. The thermal radiation was neglected since it was comparatively insignificant. In addition, in the well of multiple pay zones, the upward seepage velocity of the tubing fluid that changes with depth should be taken into account, as illustrated in Figure 2. As fluid A from the pay zone A enters the tubing, it would mix with fluid B from the lower pay zone B, hence the tubing fluid flow above the pay zone A would equal the sum of flows of fluids A and B, causing the fluid velocity to increase. The tubing fluid below the pay zone B can be assumed to be static ($v_z = 0$), thus only heat conduction was considered. In addition, we regarded the two-phase mixed flow in the tubing as a weighted single-phase flow [24].

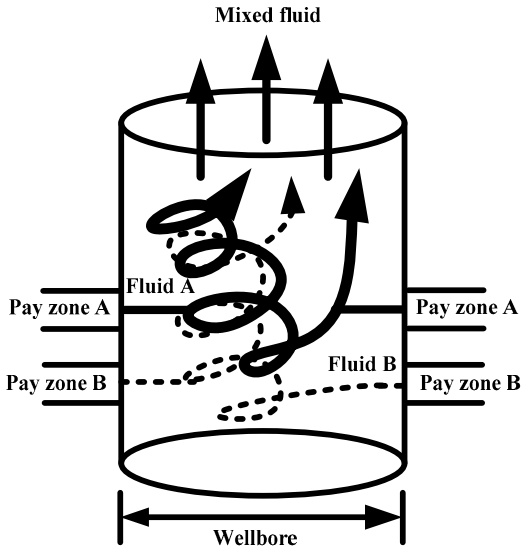


Figure 2. Schematic of two-phase fluid flow in the tubing.

2.1.3. Downhole Heat Transfer Model

The downhole temperature distribution was assumed to be axially symmetric. Hence, the 3-D model can be simplified to a 2-D one. Figure 3 depicts our 2-D coupled model in cylindrical coordinates during the exploitation process.

In order to facilitate the research, the complex downhole configuration can be divided into three layers in the horizontal direction: the fluid in the tubing; the fluid in the tubing-casing annulus.

The tubing wall, casing, cement ring and formation were divided into multiple layers according to the casing program. In addition, in the vertical direction and the wellbore-formation can be also divided into three parts: overburden; surrounding formations; pay zones.

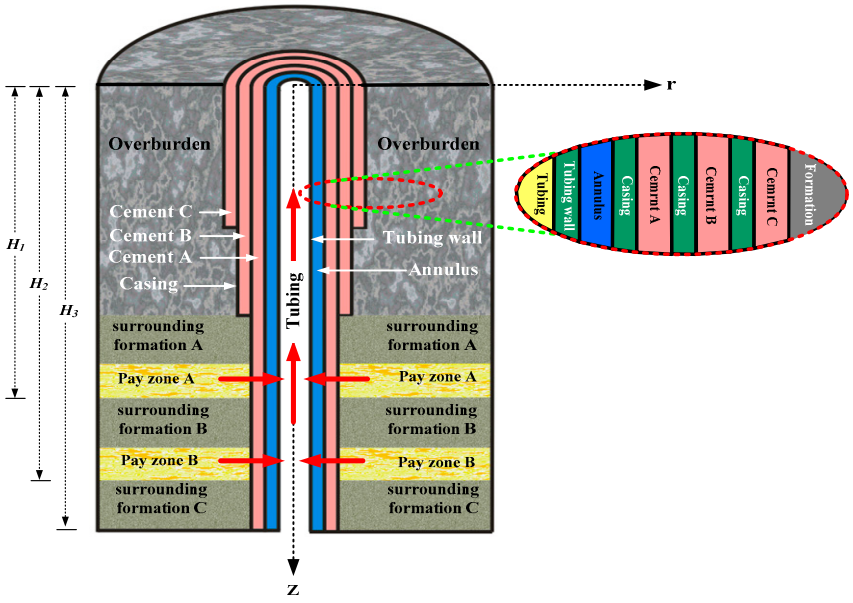


Figure 3. Schematic of the downhole temperature model.

2.1.4. Assumptions of the Model

In this downhole heat transfer model, the major assumptions and approximations are as following:

(1) Initial (undisturbed) downhole temperature distribution was a known function of depth. In addition, the thermodynamic parameters of all media did not change with temperature.
(2) Frictional heating and Joule-Thomson effect on the downhole temperature distribution were neglected.
(3) Fluid was incompressible, fluid density and viscosity were constant. In addition, the thermal properties of the mixture of the two-phase fluid in the tubing were homogenous.
(4) Pay zones and adjacent zones were isotropic and vertical borehole radius remains unchanged with depth.
(5) For pay zones, there were no fluid channeling phenomena during water drive development and the water drive process was regarded as a rigid hydrostatic drive.

2.2. Solution of the Seepage Characteristics for Pay Zones

2.2.1. Derivation of the Oil–water Two-Phase Theory Based on Plane Radial Flow

Based on the BL displacement theory, the oil–water two-phase plane radial flow (non-piston-like displacement) mathematical model was established without considering the factors of gravity and capillary pressure [31]:

$$r^2 - r_e^2 = \frac{f'_w(s_w) q_{rate} t}{\varnothing \pi h} \quad (1)$$

where $f'_w(s_w)$ represents the derivative of water cut (f_w) with respect to water saturation (s_w), and water cut (f_w) can be given by:

$$f_w(s_w) = \frac{1}{1 + \frac{\mu_w K_{ro(s_w)}}{\mu_o K_{rw(s_w)}}}. \quad (2)$$

In order to simulate the relative permeability of two-phase flow in pay zones, we applied the classic VGM model [32], which is presented by the following expression:

$$\begin{cases} K_{rw} = s_w^{1/2}\left[1-\left(1-s_w^{1/m}\right)^m\right]^2 \\ K_{ro} = s_o^{1/2}\left(1-s_w^{1/m}\right)^{2m}. \end{cases} \quad (3)$$

In Equation (3), the parameter m is given by a constant value; here, we let m = 0.8060.

A special saturation "s_{wf}" is defined as follows: as shown in Figure 4, based on the water cut curve ($f_w(s_w)$), selecting the point of irreducible water saturation (s_{wi}) as a fixed point and joining any other point on the curve, with a constructing function [31]:

$$f'_w(s_w) = \left(f_w(s_w) - f_w(s_{wi})\right)/\left(s_w - s_{wi}\right) \quad (4)$$

If Max $\{f'_w(s_w)\} = f'_w\left(s_{wf}\right)$ was found, we called "s_{wf}" the "frontier" saturation. Therefore, we derived the corresponding displacement (r_{wf}) of water drive front at different production times from Equation (1), as presented by the following equation:

$$r_{wf}^2 = \frac{f'_w(s_w)q_{rate}t}{\varnothing\pi h} + r_e^2 \quad (5)$$

We also computed the WBT (t_w) with the input of Max$\{f'_w(s_w)\} = f'_w\left(s_{wf}\right)$:

$$t_w = \frac{\left(r_e^2 - r_{ti}^2\right)\varnothing\pi h}{f'_w\left(s_{wf}\right)\left|q_{rate}\right|} \quad (6)$$

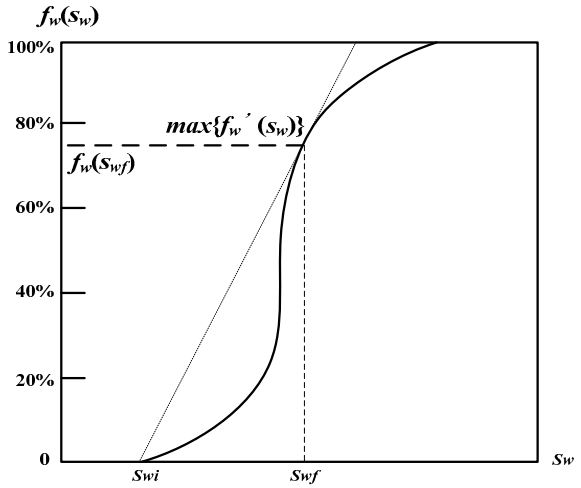


Figure 4. Schematic of water saturation of the water drive front.

2.2.2. Solution of the Water Saturation for Pay Zones

A reservoir profile grid model was established as shown in Figure 5, which was convenient to describe the relevant physical processes. In addition, the inside radius of the tubing and the reservoir limit were denoted as r_{ti} and r_e, respectively, and h was the reservoir thickness/height.

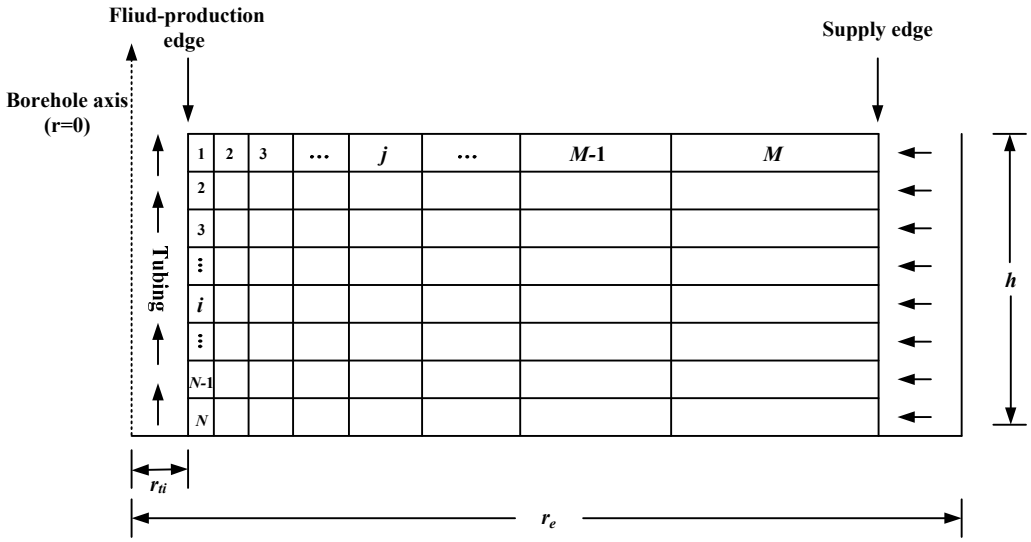


Figure 5. Schematic of the grid model for the pay zone.

In order to compute the water saturation in the pay zone at different times, the calculation steps are as follows:

Step 1: The reservoir profile grid model was established (Figure 5). The radial grid was treated with the logarithmic method, and the total number of radial grids was M. The distance between each grid node and the borehole axis ($r = 0$) was $r(j)$, where $j = 1,2,3 \ldots M + 1$.

Step 2: The values of $\emptyset$, K, s_{wi}, μ_w, μ_o, q, h and t were set. In addition, we obtained a set of water saturation values (s_{w_array}) from s_{wi} to 100% with linear interpolation by setting the water saturation step Δs_w. Then we created a relational table between $f_w(s_{w_array})$ and s_{w_array} from Equations (2) and (3), and another relational table between $f'_w\left(s_{w_array}\right)$ and s_{w_array} was generated from Equation (4).

Step3: The production time (t_w) when the water drive front reached the tubing was computed using Equation (6).

Step 4: If $t \geq t_w$, we went to step 5; if $t < t_w$, we went to steps 6 through 8.

Step 5: $F'_{sw}(s_w(\ j\ ))$ of each grid node was computed from Equation (1), we simulated the saturation $s_w(\ j\ )$ of each grid node with linear interpolation by combining $F'_{sw}(s_w(\ j\ ))$ and the relational table between $f'_w\left(s_{w_array}\right)$ and s_{w_array}. Then we ran step 8.

Step 6: The radial position (r_{wf}) of the water drive front was computed from Equation (5), and according to the specific production time (t), we obtained the grid node $j_{\max}$ ($r(j_{\max}) = r_{wf}$) of the water drive front and the water saturation (s_{wf}) of the water drive front was also obtained.

Setp 7: If $j = j_{\max}$, then $s_w(j_{\max}) = s_{wf}$; if $r(j) < r_{wf}$, then $s_w(j) = s_{wi}$; if $r(j) > r_{wf}$, we simulated the saturation $s_w(j)$ of each grid node with linear interpolation by combining $F'_{sw}(s_w(\ j\ ))$ and the relational table between $f'_w\left(s_{w_array}\right)$ and s_{w_array}.

Step 8: $s_w(M + 1) = 100\%$.

The calculation procedure of water saturation $s_w(j)$ for the pay zone is shown in Figure 6.

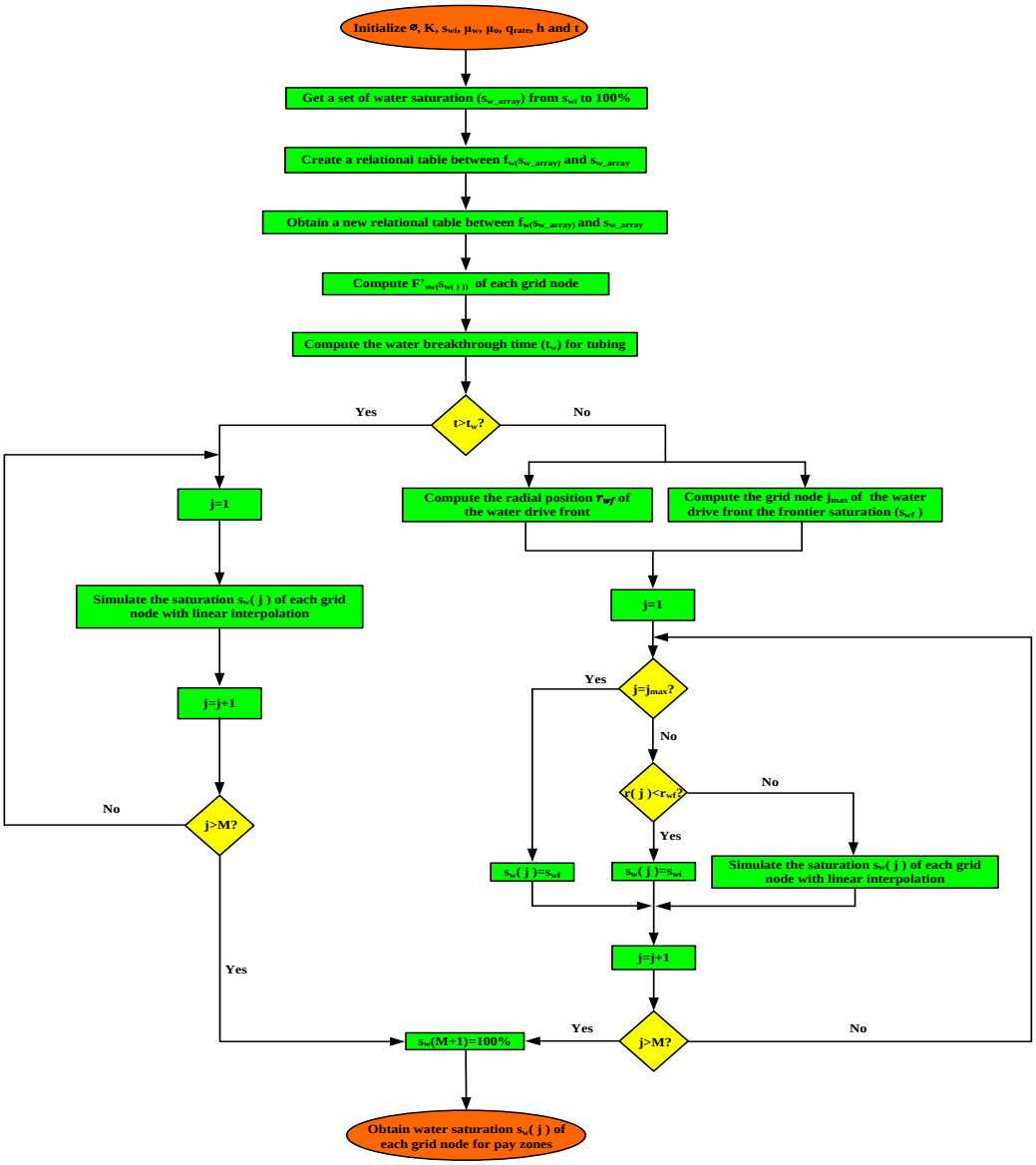


Figure 6. Flow chart of water saturation calculation for pay zones.

2.2.3. Solution of the Seepage Velocity of Two-Phase Fluid for Pay Zones

After calculating the saturation of two-phase fluid in the pay zone, the water cut (f_w) was easily acquired from Equation (2). Therefore the seepage velocity can be expressed as follows:

$$\begin{cases} v_{wr} = q_w/(\varnothing A(r)) \\ v_{or} = q_o/(\varnothing A(r)) \end{cases} \tag{7}$$

where·

$$q_w = q_{rate} f_w \tag{8}$$

$$q_o = q_{rate} f_o \tag{9}$$

$$q_{rate} = q_w + q_o \tag{10}$$

$$A(r) = 2\pi rh. \tag{11}$$

2.2.4. Solution of the Pressure for Pay Zones

As the gravitation effect and the capillary pressure were not considered in this model, based on a 1-D plane radial flow, an equation set for immiscible displacement in cylindrical coordinates can be described by [29,33]:

$$\begin{cases} v_{wr} = -\Lambda_w \frac{dP}{dr} \\ v_{or} = -\Lambda_o \frac{dP}{dr} \end{cases} \tag{12}$$

where

$$\begin{cases} \Lambda_w = kk_{rw}/\mu_w \\ \Lambda_o = kk_{ro}/\mu_o \end{cases}. \tag{13}$$

We assumed the flow rate (q_{rate}) remained constant for the pay zones in this model, hence we combined Equations (7), (10) and (12) to yield the partial differential equation for the pressure of the two-phase system in the pay zone:

$$\frac{\partial P}{\partial r} = \frac{q_{rate}}{-\Lambda A(r)} \tag{14}$$

where

$$\Lambda = \Lambda_w + \Lambda_o = kk_{rw}/\mu_w + kk_{ro}/\mu_o. \tag{15}$$

Based on the reservoir profile grid model (Figure 5), we noticed that $dr = rdx$ (the detailed derivation is shown in Appendix A), hence Equation (14) was derived as follows in the Cartesian coordinate system:

$$\frac{\partial P}{\partial x} = -\frac{q_{rate}}{2\pi h \Lambda} \tag{16}$$

The discrete form for Equation (16) is shown in Appendix B.

2.3. Transient Temperature Governing Equation of Coupled Two-Phase Fluid Flow and Heat Transfer Model

According to the downhole heat transfer model, the corresponding temperature field control equation can be derived. In this study, the five-point implicit difference method was used to solve the temperature distribution and the finite difference discrete schemes of the model are presented in Appendix B.

2.3.1. Heat Transfer Model Inside the Tubing

We considered the heat transfer of a fluid in vertical tubing as a continuous medium conduction and convection during the exploitation process. Only the vertical component was considered and the radial component was neglected for the fluid velocity. Therefore, the heat transfer equation in the tubing can be written as:

$$\nabla \cdot (\lambda_l \nabla T) = \frac{\partial}{\partial t}\Big((\rho c)_l T\Big) + \nabla\Big((\rho c)_l v_z T\Big). \tag{17}$$

The downhole temperature distribution was assumed to be axialyl symmetric in this study, thus Equation (17) was reduced to:

$$\frac{1}{r}\frac{\partial}{\partial x}\left(r\lambda_l \frac{\partial T}{\partial x}\right) + \frac{\partial}{\partial z}\left(\lambda_l \frac{\partial T}{\partial z}\right) - \frac{\partial}{\partial z}\Big((\rho c)_l v_z T\Big) = \frac{\partial}{\partial t}\Big((\rho c)_l T\Big) \tag{18}$$

where

$$\lambda_l = f_w \lambda_w + (1 - f_w)\lambda_o \tag{19}$$

$$(\rho c)_l = f_w \rho_w c_w + (1 - f_w)\rho_o c_o. \tag{20}$$

In Equation (18), the upward seepage velocity (v_z) of the fluid inside the tubing was defined as:

$$v_z = \begin{cases} \frac{q_{rate}}{\pi r_{ti}^2}, & \text{if } 0 < Z_i \le H_1 \\ \frac{q_{rate}}{\pi r_{ti}^2} P_B, & \text{if } H_1 < Z_i \le H_2 \\ 0, & \text{if } H_2 < Z_i \le H_3 \end{cases} \tag{21}$$

where H_1 represents the depth of the bottom of the pay zone A, H_2 means the depth of the bottom of the pay zone B, H_3 is the total well depth from the surface. In addition, they are presented in Figure 3.

2.3.2. Heat Transfer Model from the Adjacent Formations to the Tubing Wall

Heat conduction dominated the heat transfer of the adjacent formation regions above and below the pay zones [34]. In addition, in order to facilitate the research, we assumed the tubing-casing annulus was filled with static water and ignored its thermal radiation effects. Thus the transient temperature field governing equation for the tubing wall, tubing-casing annulus, casing, cement, overburden and surrounding formations can be given by:

$$\nabla\cdot\left(\lambda_{s1}^{*}\nabla T\right) = \frac{\partial}{\partial t}\left((\rho c)_{s1}^{*}T\right). \tag{22}$$

For the 2-D temperature field model, Equation (22) becomes:

$$\frac{1}{r}\frac{\partial}{r\partial x}\left(r\lambda_{s1}^{*}\frac{\partial T}{r\partial x}\right) + \frac{\partial}{\partial z}\left(\lambda_{s1}^{*}\frac{\partial T}{\partial z}\right) = \frac{\partial}{\partial t}\left((\rho c)_{s1}^{*}T\right) \tag{23}$$

where

$$\lambda_{s1}^{*} = \lambda_{s1}^{1-\varnothing_1}\left(\lambda_w s_w + \lambda_o s_o\right)^{\varnothing_1} \tag{24}$$

$$(\rho c)_{s1}^{*} = \varnothing_1(\rho_w c_w s_w + \rho_o c_o s_o) + (1-\varnothing_1)\rho_{s1}c_{s1}. \tag{25}$$

2.3.3. Heat Transfer Model of Pay Zones

The heat convection and conduction of a fluid in the pay zones dominated the heat transfer of reservoir porous media so we expressed the temperature field equation of the pay zones as:

$$\nabla\cdot\left(\lambda_{s2}^{*}\nabla T\right) = \frac{\partial}{\partial t}\left((\rho c)_{s2}^{*}T\right) + \nabla\left((\rho cv)_r T\right). \tag{26}$$

In the same way, Equation (26) was reduced to:

$$\frac{1}{r}\frac{\partial}{r\partial x}\left(r\lambda_{s2}^{*}\frac{\partial T}{r\partial x}\right) + \frac{\partial}{\partial z}\left(\lambda_{s2}^{*}\frac{\partial T}{\partial z}\right) - \frac{\partial}{r\partial x}\left((\rho cv)_r T\right) = \frac{\partial}{\partial t}\left((\rho c)_{s2}^{*}T\right) \tag{27}$$

where

$$\lambda_{s2}^{*} = \lambda_{s2}^{1-\varnothing_2}\left(\lambda_w s_w + \lambda_o s_o\right)^{\varnothing_2} \tag{28}$$

$$(\rho c)_{s2}^{*} = \varnothing_2(\rho_w c_w s_w + \rho_o c_o s_o) + (1-\varnothing_2)(\rho_{s2}c_{s2}) \tag{29}$$

$$(\rho cv)_r = \rho_o c_o s_o v_{or} + \rho_w c_w s_w v_{wr}. \tag{30}$$

2.4. Initial and Boundary Conditions

2.4.1. Initial and Boundary Conditions of Water Saturation and Pressure for the Pay Zones

In the pay zones, the initial water saturation was considered as a fixed value, which can be formulated as Equation (31). The water saturation of the inner boundary of the water drive reservoir changed with the production time, while the water saturation of the outer boundary was considered to

be 100% at any production time because the outer boundary was the water supply edge, which was expressed as Equation (32).

$$s_w(r,t)\big|_{t=0} = s_{wi} \tag{31}$$

$$s_w(r,t)\big|_{r=r_e} = 100\%. \tag{32}$$

The initial pressure for the pay zones was given by a constant, which can be defined by Equation (33). The inner boundary condition of the pressure for water drive reservoir can be classified into two major forms: (1) flow rate (q_{rate}) remains constant; (2) the bottom-hole pressure was considered to be a certain value. We considered the former type in this model, the inner boundary condition of the pressure was, therefore, given by Equation (34). In addition, the outer boundary condition of the pressure was calculated by Equation (35).

$$P(r,t)\big|_{t=0} = P_0 \tag{33}$$

$$Q = -2\pi r h \frac{k}{\mu}\frac{\partial P}{\partial n}|_{r=r_{ti}} \tag{34}$$

$$P(r,t)\big|_{r=r_e} = P_{ref} + g_P z. \tag{35}$$

2.4.2. Initial and Boundary Conditions of Downhole Temperature

We assumed the initial temperature was the undisturbed geothermal condition. Thus, the initial condition of downhole temperature can be written as:

$$T|_{t=0} = T_{sur} + g_T z \tag{36}$$

In the radial direction, the adiabatic boundary condition at the borehole axis can be described as Equation (37), the dynamic coupled boundary conditions of temperature at the interfaces between the tubing fluid and the tubing wall, the tubing fluid and the pay zones can be described as Equations (38) and (39), respectively. The formation temperature of the outer boundary was equal to the undisturbed geothermal temperature when the reservoir limit (r_e) was sufficiently large. Therefore its boundary condition is given in Equation (40).

$$\lambda_l \frac{\partial T}{\partial r}|_{r=0} = 0 \tag{37}$$

$$\begin{cases} h_c(T_{l1} - T_{s1}) = -\lambda^*_{s1}\frac{\partial T}{\partial r}|_{r=r_{ti}} \\ T_{l1}|_{r=r_{ti}} = T_{s1}|_{r=r_{ti}} \end{cases}. \tag{38}$$

$$\begin{cases} \lambda_l \frac{\partial T}{\partial r}|_{r=r_{ti}} + |(\rho c v)_r|(T_{s2} - T_{l2})|_{r=r_{ti}} = \lambda^*_{s2}\frac{\partial T}{\partial r}|_{r=r_{ti}} \\ T_{l2}|_{r=r_{ti}} = T_{s2}|_{r=r_{ti}} \end{cases} \tag{39}$$

$$T|_{r=r_e} = T_{sur} + g_T z. \tag{40}$$

In Equation (38), h_c is the convection heat transfer coefficient. Combining the Dittus-Boelter equation ($N_{uf} = 0.023 R_{ef}^{0.8} P_{rf}^{n}$) and the definition of Nusselt number ($N_{uf} = h_c L/\lambda_f$), the heat transfer coefficient by convection was obtained by the following:

$$h_c = 0.023\frac{\lambda_f}{L} R_{ef}^{0.8} P_{rf}^{n}. \tag{41}$$

In Equation (41), where λ_f is the thermal conductivity of the fluid, L is the characteristic length. In addition, n = 0.4 for the fluid being heated, n = 0.3 for the fluid being cooled. Here, we let n = 0.3.

In the longitudinal direction, we further assumed that no heat transfer occurred at the top and bottom of the wellbore-formation. Thus their boundary conditions of temperature can be written as

Equations (42)–(45). In addition, the dynamic coupled boundary conditions of temperature at the interfaces between the pay zones and adjacent formations can be described by Equation (46).

$$\lambda_l \frac{\partial T}{\partial z}|_{z=0(r\le r_{ti})} = 0 \tag{42}$$

$$\lambda^*_{s1} \frac{\partial T}{\partial z}|_{z=0(r_{ti}<r\le r_e)} = 0 \tag{43}$$

$$\lambda_l \frac{\partial T}{\partial z}|_{z=z_{max}}(r \le r_{ti}) = 0 \tag{44}$$

$$\lambda^*_{s1} \frac{\partial T}{\partial z}|_{z=z_{max}}(r_{ti} < r \le r_e) = 0 \tag{45}$$

$$\begin{cases} \lambda^*_{s1} \frac{\partial T}{\partial z}\Big|_{z=z_b}(r_{ti} < r \le r_e) = \lambda^*_{s2} \frac{\partial T}{\partial z}\Big|_{z=z_b}(r_{ti} < r \le r_e\ ) \\ T_{bl}\Big|_{z=z_b} = T_{bs}\Big|_{z=z_b} \end{cases} \tag{46}$$

3. Model Comparison

The proposed model (numerical solution) was programmed and compared with the classic Hasan analytical model [35] to ensure that no error was made in the mathematical equations in the solution and computer modeling.

3.1. Analytical Solution of the Simplified Model

The derivations of the Hasan model and our proposed model were dependent on the same concepts and production form. Thus, the simplified model was designed and built to verify the accuracy of the proposed model in this paper. As is illustrated in Figure 7, the simplified model consisted of the wellbore, overburden and a pay zone.

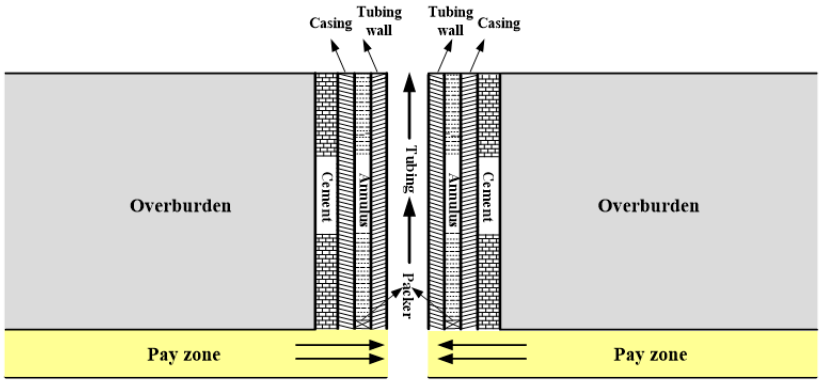


Figure 7. Schematic of downhole configuration for the simplified model.

The classic Hasan model was derived from the total-energy-balance equation. Thus for a producing well, fluid and formation temperatures ($T_f = T_{fbh}$ and $T_{ei} = T_{eibh}$) were generally known at the bottom-hole ($z = z_{bh}$). We can give the following expression for fluid temperature as a function of well depth and producing time [35]:

$$T_f = T_{ei} + A\left[1 - e^{\left(\frac{z_{bh}-z}{A}\right)}\right]\left(-\frac{gsin\theta}{g_c J c_{pm}} + \varphi + g_T sin\theta\right) + e^{\left(\frac{z_{bh}-z}{A}\right)}\left(T_{fbh} - T_{eibh}\right) \tag{47}$$

where

$$\mathrm{A} = \frac{c_{pm} w}{2\pi}\left(\frac{k_e + r_{to} U_{to} f(t_D)}{r_{to} U_{to} k_e}\right) \tag{48}$$

$$\frac{1}{U_{to}} = \frac{r_{to}}{r_{ti}h_{to}} + \frac{r_{to}ln(r_{to}/r_{ti})}{k_t} + \frac{1}{h_{uc}+h_{ur}} + \frac{r_{to}ln(r_{co}/r_{ci})}{k_{cas}} + \frac{r_{to}ln(r_{wb}/r_{co})}{k_{cem}}. \quad (49)$$

In Equation (48), $f(t_D)$ was computed by an algebraic, which is a function of the dimensionless time (t_D). In this study, we applied a hybrid approach to estimate $f(t_D)$ taking into account the existing models [9,36–38], based on the t_D, as follows [6]:

$$f(t_D) = \begin{cases} 1.1281\sqrt{t_D}\left(1-0.3\sqrt{t_D}\right) & \text{if } t_D \le 0.5 \\ ln\left(2\sqrt{t_D}-0.2886\right)+\frac{1}{4t_D}\left[1+\left(1-\frac{1}{c_r}\right)\ln(4t_D)+0.5772\right] & \text{if } 0.5 < t_D \le 20 \\ ln\left(2\sqrt{t_D}\right)-0.2886 & \text{if } t_D > 20 \end{cases} \quad (50)$$

where

$$t_D = \frac{\alpha_{ft}t}{r_{wb}^2} \quad (51)$$

$$c_r = \frac{(\rho c)_{s1}^*}{(\rho c)_l}. \quad (52)$$

3.2. Temperature Comparative Analysis of the Proposed Model and Hasan Analytical Solution

The downhole geometry parameters and ambient temperature are given in Table 1. In addition, the results from the proposed model and the Hasan analytical model were compared with a typical data set, the data used in the models are provided in Tables 2 and 3. In addition, we assume the flow rate (q_{rate}) of the wellhead was 61.07 m^3/d, we computed a WBT value of 76.74 days using our proposed model. Therefore the fluid temperature profiles for the production time were greater or less than 76.74 days and were selected for comparison.

Table 1. Downhole geometry and ambient temperature.

Properties	Value
Inside radius of tubing (r_{ti})/m	0.05
Outside radius of tubing (r_{to})/m	0.06
Inside radius of casing (r_{ci})/m	0.07
Outside radius of casing (r_{co})/m	0.08
Outside radius of cement (r_{wb})/m	0.09
Reservoir limit (r_e)/m	27.40
Thickness of the overburden (h_{over})/m	1475
Thickness of pay zone (h)/m	25
Surface temperature (T_{sur})/°C	20
Geothermal gradient (g_T)/°C/m	0.03

Table 2. Fluids properties.

Properties \ Material	Water	Oil
Density/kg/m^3	1000	800
Specific heat/[J/(Kg·°C)]	4220	1920
Thermal conductivity coefficient/[W/(m·°C)]	0.622	0.148
Dynamic viscosity/Pa s	0.00068	0.0034

Table 3. Data used in model comparison.

Properties \ Material	Tubing (Casing)	Cement	Overburden	Matrix of the Pay Zone
Density/kg/m^3	7900	2150	1920	2650
Specific heat/[J/(Kg·°C)]	460	2000	922	850
Thermal conductivity coefficient /[W/(m·°C)]	16.2	0.7	1.02	2.1
Thermal diffusion coefficient/m^2/s	-	-	1.03×10^{-6}	-
Porosity/%	-	-	-	15
Absolute permeability/μm^2	-	-	-	0.1
Irreducible water saturation /%	-	-	-	20

The temperature profiles of these two models with different production times given are presented in Figure 8. The results matched well with each other and the absolute value of the maximum temperature difference was less than 0.5 °C, which indicated the validity of the mathematical derivation. Besides that, because the convective heat transfer of pay zone was taken into account in the proposed model, we noticed that the tubing fluid temperature calculated by our proposed model in the section of the pay zone (1475 m $\leq z \leq$ 1500 m) was higher than that of Hasan analytical solution during the entire production life.

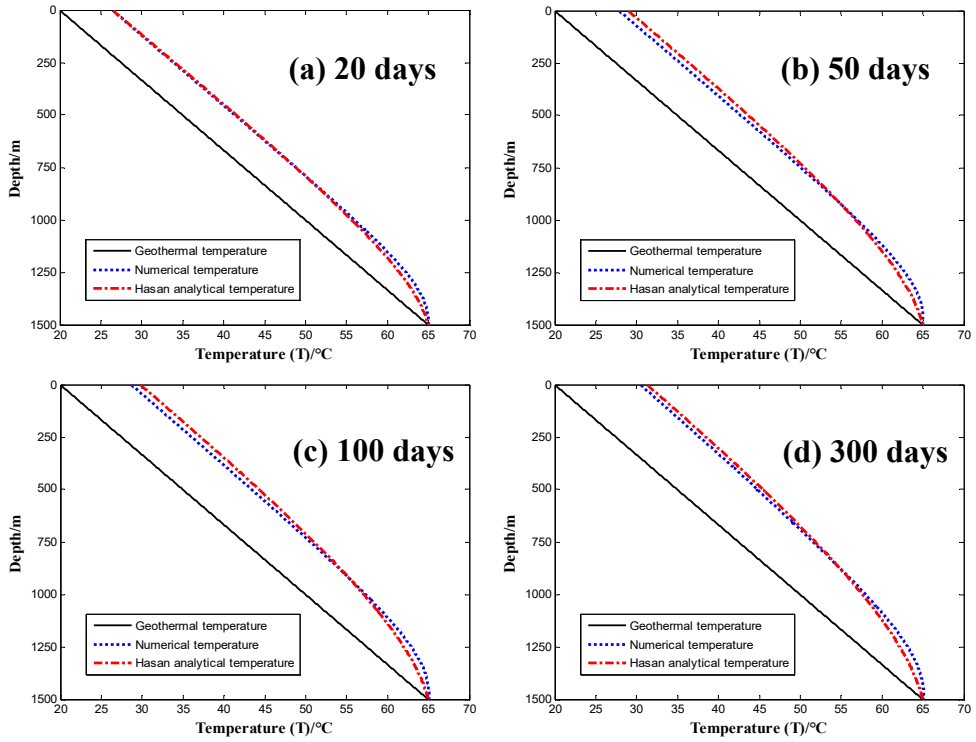


Figure 8. Comparison of the temperature profile of the proposed model with a Hasan analytical solution at different production times. (**a**), (**b**), (**c**), (**d**) are the temperature profiles of 20, 50, 100, 300 days of production time, respectively.

Further comparison was conducted to verify the proposed model, the relative errors between the two models are analyzed, and the relative error expression was constructed as follows:

$$R_{error} = \left(T_{num} - T_{analy}\right)/T_{analy}. \quad (53)$$

The details of the error analysis are shown in Figure 9. The results show good agreement with an average difference of less than 2.0%. In addition, the temperature difference between the proposed

model and analytical solution due to the following two main reasons: (1) The numerical method took into account the seepage effects of the pay zone, while the Hasan analytical model only considered the heat transfer of the wellbore fluid; (2) the radiant heat of the tubing-casing annulus and the Joule-Thomson effect on the fluid temperature distribution were neglected for the proposed model, but Hasan analytic model considered these factor.

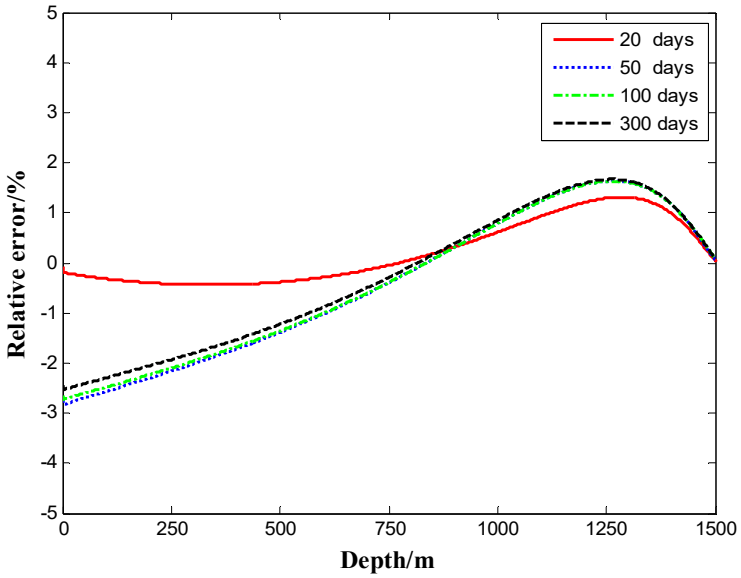


Figure 9. Error analysis of the temperature of proposed model and Hasan analytical solution with different production times.

4. Results and Discussion

A novel method was proposed to simulate the seepage characteristics of pay zones. Then, combining the prescribed initial and boundary conditions, an implicit finite difference method was used to compute the transient temperature with the input of the seepage characteristics for reservoir fluid, and the calculation method of the five-point implicit difference is shown in Appendix C. Finally, a sensitivity analysis was used to study the influences of production rate (q_{rate}), production time (t) on the tubing fluid temperature distribution (r = 0.04 m, 0 m $\leq$ z $\leq$ 1100 m), to analyze the effects from the volumetric heat capacity (VHC) and the thermal conductivity (TC) for the overburden temperature distribution (r = 0.14 m, 0 m $\leq$ z $\leq$ 1000 m). A further study showed the effects of the porosity ($\emptyset$) and the irreducible water saturation (s_{wi}) of pay zones on the formation temperature variation (r = 0.14 m, 1000 m $\leq$ z $\leq$ 1100 m).

The modeled region consisted of the wellbore with production fluid flow, overburden and the surrounding formations with two pay zones, and we assumed the lithology of the reservoir was homogeneous and isotropic. The geometry parameters of the model are given in Table 4. In addition, the downhole mesh generation method is shown in Appendix A. The fluid (water and oil) properties were identical with Table 2, the physical parameters for wellbore, overburden and matrix of pay zones were the same as in Table 3, and the other required reservoir properties are listed in Table 5. In addition, the total flow rate (q_{rate}) of the wellhead was set to be 169.65 m^3/d, the ratio of the flow rate of pay zone A (or pay zone B) to the total flow ratewas 50% (P_A = P_B = 50%), and we computed that the WBT was 522.05 days with the above parameters in our proposed model.

Table 4. Downhole geometry parameters.

Radial direction	
Inside radius of tubing (r_{ti})/m	0.050
Outside radius of tubing (r_{to})/m	0.055
Inside radius of casing (r_{ci})/m	0.065
Outside radius of casing (r_{co})/m	0.070
Outside radius of cement A (r_{ab})/m	0.090
Outside radius of cement B (r_{bb})/m	0.110
Outside radius of cement C (r_{cb})/m	0.130
Reservoir limit (r_e)/m	266.29
Longitudinal direction	
Interval of cement A/m	0–1100
Interval of cement B/m	0–1000
Interval of cement C/m	0–500
Interval of overburden /m	0–1000
Interval of surrounding formation A/m	1000–1030
Interval of pay zone A/m	1030–1035
Interval of surrounding formation B/m	1035–1065
Interval of pay zone B/m	1065–1070
Interval of surrounding formation C/m	1070–1100

Table 5. Reservoir properties.

Surrounding Formations A, B and C	
Density (ρ_{s1})/Kg/m^3	2450
Specific heat (c_{s1})/[J/(Kg·°C)]	820
Thermal conductivity coefficient (λ_{s1})/[W/(m·°C)]	2.25
Porosity ($\emptyset_1$)/%	15
Water saturation (s_{fi})/%	20
Ambient temperature	
Surface temperature (T_{sur})/°C	20
Geothermal gradient (g_T)/°C/m	0.03

4.1. Seepage Characteristics in Pay Zones

4.1.1. Saturation, Seepage Velocity of Oil–Water Two-Phase Fluid in Pay Zones

Figure 10 shows the seepage characteristics of two-phase flow in pay zones with different production times. In addition, we obtained the following cognitions:

(1) The saturation (s_w) and seepage velocity (v_{wr}) of water phase all increased with the production time, however, the saturation (s_o) and seepage velocity (v_{or}) of the oil phase were negatively correlated with the production time.

(2) When the production times were 50 days and 100 days (50 days < t_w, 100 days < t_w, t_w = 522.05 days), the radial distance (r_{wf}) from the borehole axis to the water drive front was 253.29 m and 239.50 m, respectively; we obtained the "frontier" water saturation (s_{wf}) of both as 62%. In addition, the range from the reservoir limit (r_e = 266.29 m) to the water drive front was the oil–water two-phase flow, however beyond this range (between the inside radius of the wellbore (r = 0.09 m) and the water drive front), there was no movable water. Therefore the water saturation was equal to the irreducible water saturation (s_{wi} = 20%) and there was no seepage of the water phase in this range.

(3) When the production time was 1000 days and 1500 days (1000 days > t_w, 1500 days > t_w, t_w = 522.05 days), the water drive front reached the tubing. Thus from the reservoir limit to the inside radius of the wellbore, the variation trend of the saturation and seepage velocity of oil–water two-phase fluid was gradual, and there no "steep drop" existed like the production time of 50 days or 100 days.

(4) The saturation of the water phase at reservoir limit was 100% because the reservoir limit was at the water supply edge. In addition, from the reservoir limit to the inside radius of the wellbore, the seepage velocity of oil–water two-phase fluid increased during the entire production life.

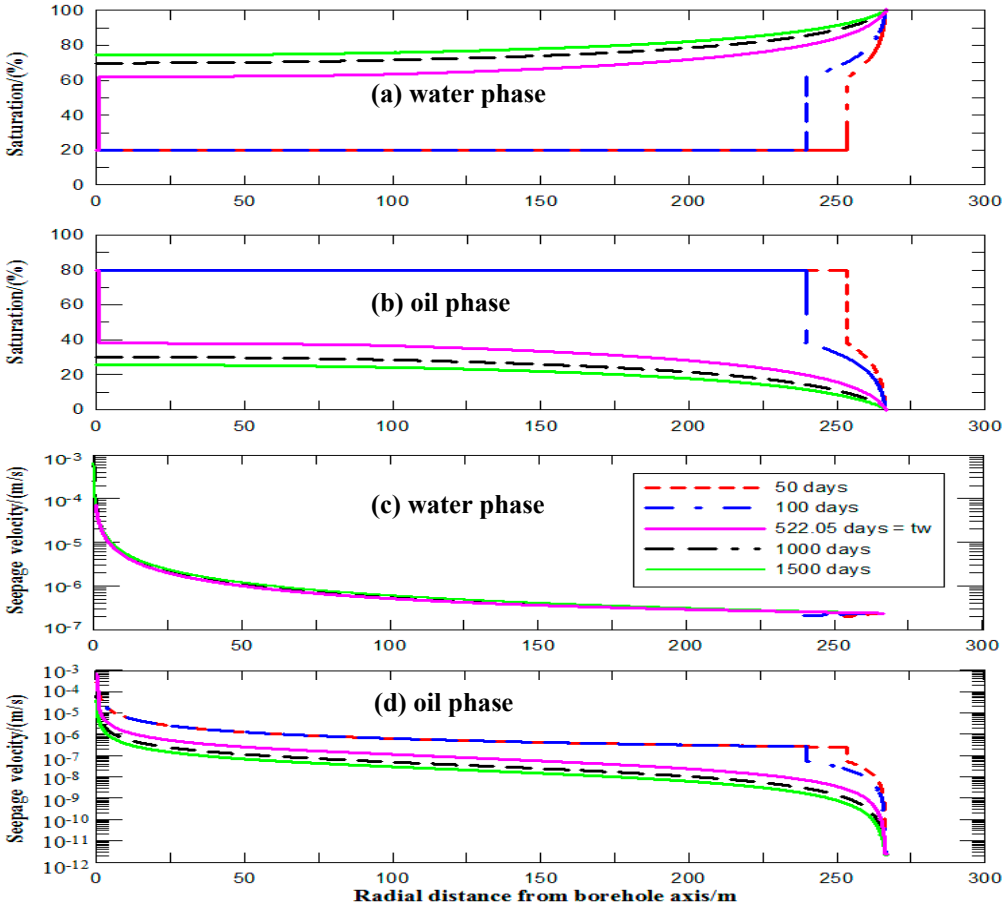


Figure 10. Water phase seepage characteristics for pay zones of oil–water two-phase flow with different production time: (**a**) water saturation; (**b**) oil saturation; (**c**) radial seepage velocity of water phase; (**d**) radial seepage velocity of the oil phase.

4.1.2. The Pressure (P) for Pay Zones of Two-Phase System

Figure 11 shows the evolution of pressure distribution (P) of the pay zones during the 1500-day production period. In addition, we obtained the following cognitions:

(1) The pressure of the pay zones was positively correlated with the production time. In addition, whether before or after the WBT (t_w = 522.05 days), the pressure drop near the reservoir limit was smaller, while it was larger near the wellbore.

(2) In this model, the inner boundary condition of the pressure for the water drive reservoir was regarded as a constant fluid output and the outer boundary condition was assumed to keep the pressure in a constant state. Therefore, the pressure value at the inner radius of the wellbore (r = 0.09 m) changed with the production time, but the pressure value was 10 MPa for the reservoir limit (r_e = 266.29 m) at any production time.

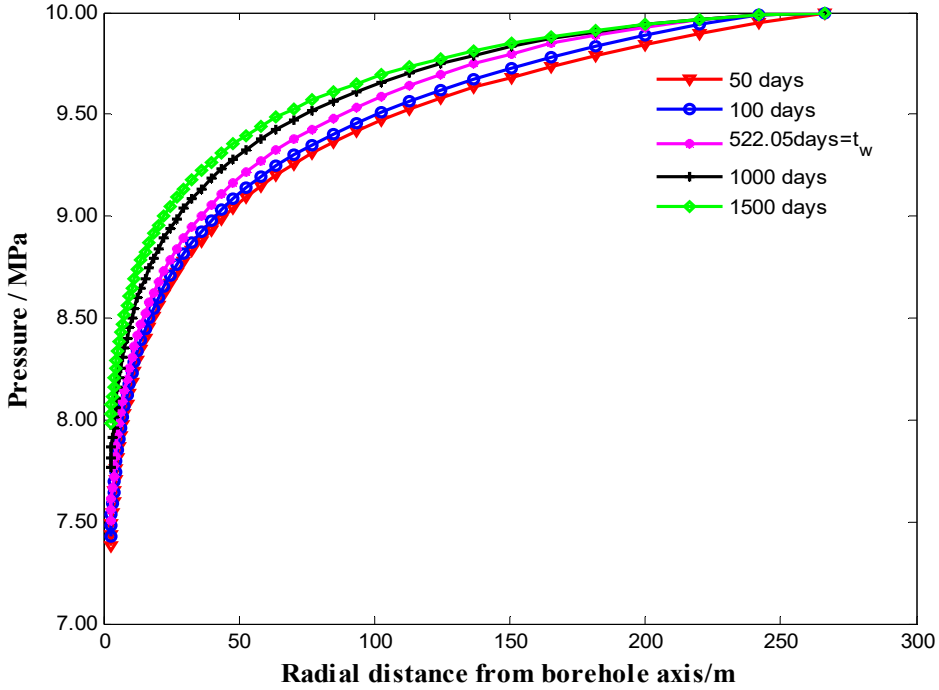


Figure 11. Pressure distribution (P) of the pay zones with different production period.

4.2. Spatial Distribution of the Downhole Temperature Variation Near Wellbore Area (1000 m ≤ z ≤ 1100 m, −2.06 m ≤ r ≤ 2.06 m)

Figure 12 shows the evolution of the spatial distribution of the downhole temperature variation near wellbore area in the section of 1000 m through 1100 m (1000 m ≤ z ≤ 1100 m, −2.06 m ≤ r ≤ 2.06 m) during the 1500 day period. In addition, we obtained the following cognitions:

(1) Wellbore and surrounding rock areas were easily identified by the downhole temperature variations. During the tubing fluid upward seepage, there was a difference in temperature between the high-temperature fluids (from the lower pay zones) and the surrounding formations A (1000 m ≤ z ≤ 1030 m) or B (1035 m ≤ z ≤ 1065 m), hence the surrounding formations were heated and the temperature rises. In addition, the spatial distribution of temperature variation of the surrounding formations A and B became more and more like a "cup". The thermal conduction effect of the tubing fluid decreased gradually in the radial direction, thus the temperature variation of the surrounding formations A and B near the wellbore was significantly bigger than that far away from the wellbore at any depth. Figure 12g–i reveals that the temperature gradually increased during the entire production life, but it did not increase indefinitely. Instead, a "saturation state" appeared.

(2) The heat convection and conduction of the wellbore fluid dominated the heat transfer of the surrounding formations A and B. Hence, the spatial distribution of temperature change presented as "cup-shaped". However, for the surrounding formation C (1070 m ≤ z ≤ 1100 m), the tubing fluid was assumed to be static (v_z = 0) in this section, hence, the longitudinal heat conduction dominated the heat transfer of the surrounding formation C. Thus, the distribution of temperature variation was "stratiform", as shown in Figure 13. The temperature change at the late stage of production (Figure 13c,d) was greater than the early stage (Figure 13a,b) and the temperature of the upper part of the surrounding rock increased (the temperature change was positive) while that of the lower part decreased (the temperature change was negative).

(3) As for the pay zones, the fluids flow from the reservoir limit (r_e = 266.29 m) to the tubing (r = 0.09 m), the adjacent formation regions above the pay zones were heated by the high-temperature fluid of the pay zones, arousing the temperature of the pay zones decreased (the temperature change was negative). We noticed that it was easier to identify pay zone A (1030 m ≤z ≤ 1035 m) than pay zone B (1065 m ≤ z ≤ 1070 m). That was because the adjacent formation regions above and below

pay zone A were heated by the tubing hot fluid. Thus, the temperature variation of pay zone A (the temperature change was negative) and the temperature variation of the adjacent formations above and below pay zone A (the temperature change was positive) were in sharp contrast. However, for pay zone B, the adjacent formation regions above pay zone B were heated by the high-temperature fluid in the tubing; however, the longitudinal heat conduction dominated the heat transfer of the adjacent formation below pay zone B (1070 m < z < 1100 m, the upper part of the surrounding formation C), and only at the late stage of production the temperature changed significantly (the temperature change was positive), therefore the section of pay zone B became relatively obvious. In addition, it was easier to identify the pay zones at the late stages than the early stages of production from the spatial distribution of temperature change.

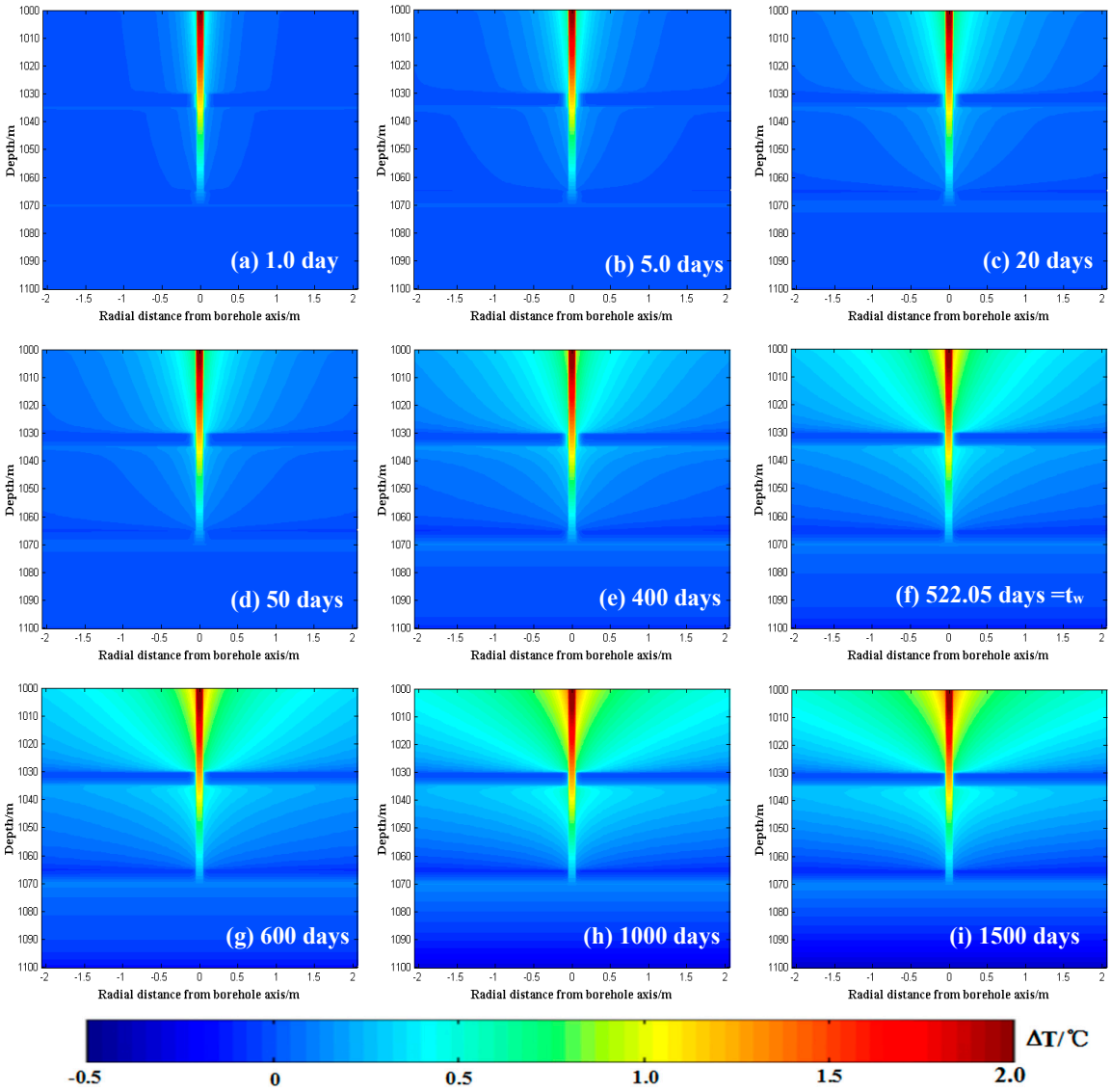


Figure 12. Evolution of the spatial distribution of the downhole temperature variation near the wellbore area (1000 m ≤ z ≤ 1100 m, -2.06m ≤ r ≤ 2.06 m) during the 1500 day period. (**a**–**i**) represent the temperature distribution from 1 day to 1500 days.

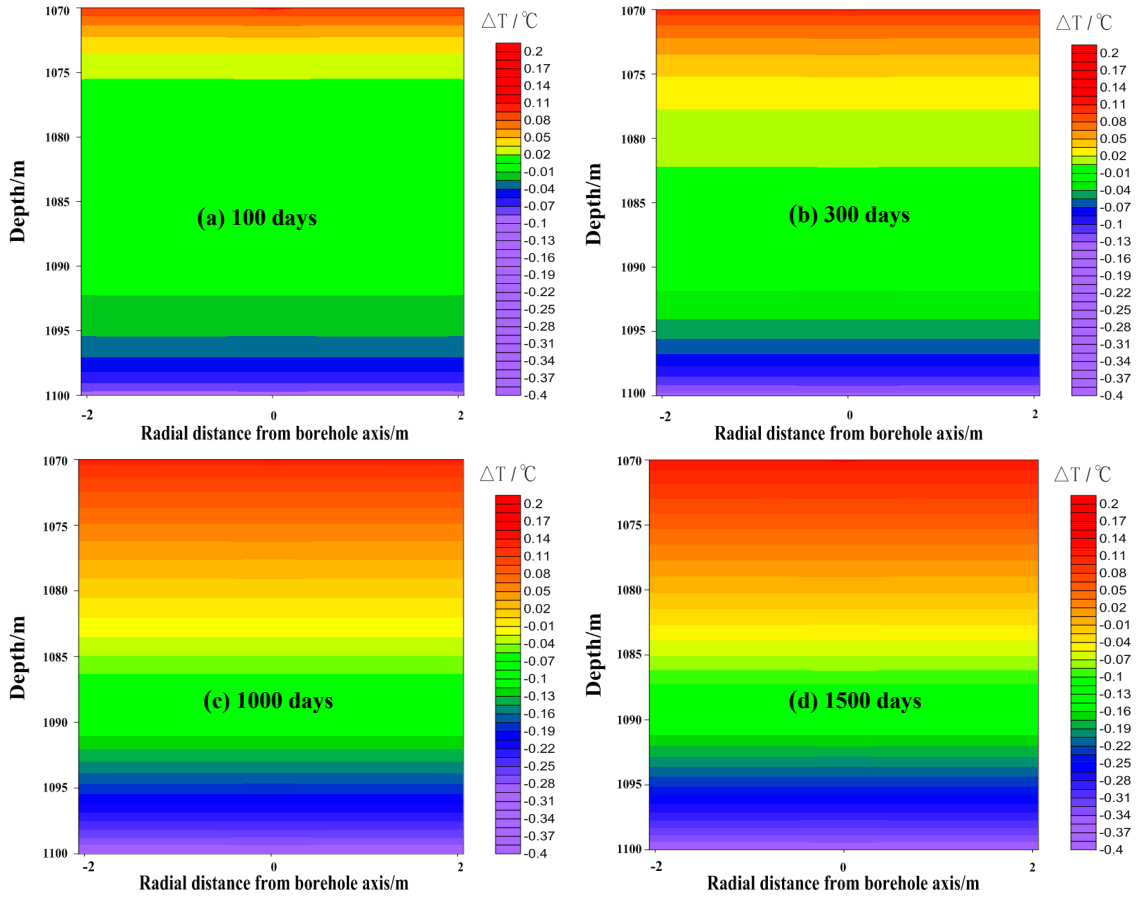


Figure 13. Evolution of the spatial distribution of the temperature variation of the surrounding formation C (1070m $\leq$ z $\leq$ 1100 m, −2.06 m $\leq$ r $\leq$ 2.06 m) during the 1500 day period. (**a**), (**b**), (**c**), (**d**) are the temperature distribution of 100, 300, 1000, 1500 days of production time, respectively.

4.3. Tubing Fluid Temperature Change

The tubing fluid temperature change at the tubing/tubing wall interface (r = 0.04 m, 1000 m $\leq z \leq$ 1070 m) with different production times (t) is shown in Figure 14. We noticed that the slope of the curve almost always approached the geothermal gradient (g_T = 0.03 °C/m). In addition, at any depth (z), the tubing fluid temperature change was close to the difference between the virgin fluid temperature at the bottom of pay zone B ($T_{sur} + 1070g_T$) and the initial geothermal temperature with different depth ($T_0 = T_{sur} + g_T z$). The temperature variation increased with the production time; thus, at the late stage of production, the tubing fluid temperature change at the depth of 1000 m was almost equal to 2.1 °C ($2.1 = (1070 - 1000) \times 0.03$).

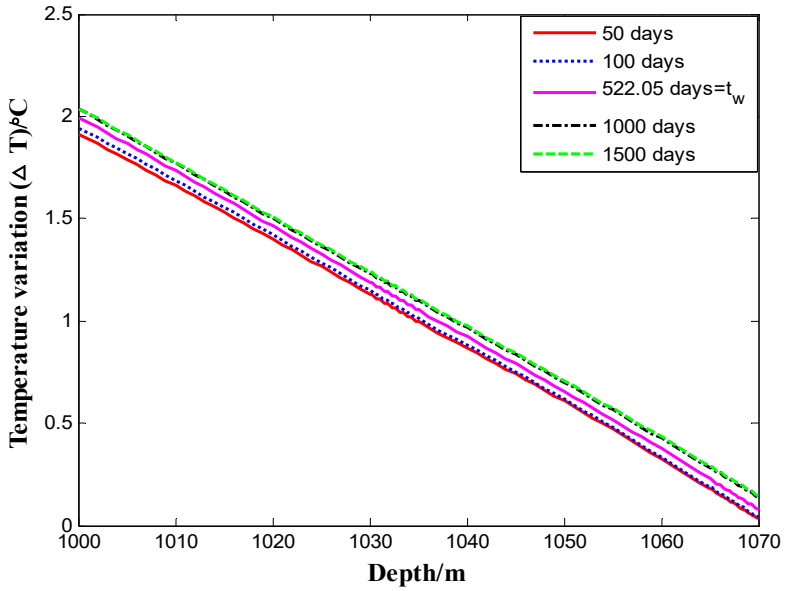


Figure 14. Tubing fluid temperature changes at the tubing-tubing wall interface (r = 0.04 m, 1000 m ≤ z ≤ 1070 m) with different production time (t).

4.4. Sensitivity Analysis

4.4.1. Sensitivity to the Production Time (t)

Figure 15 shows the sensitivity of fluid temperature in vertical tubing (r = 0.04 m, 0 m ≤ z ≤ 1100 m) to the production time (t) ranging from 1.0 day to 1500 days. The result indicates that the more distinct of the separation between the tubing fluid temperature curve and the initial (geothermal) temperature with the production times. And in the early stage of the production ($t \leq t_w$ = 522.05 days), the tubing fluid temperature changed relatively significantly with the production time, while in the late stage of production ($t > t_w$ = 522.05 days), the temperature gradually reached to a stable state, so the tubing fluid temperature barely changed. In addition, we can notice that the curves of 1000 days and 1500 days nearly overlapped, which states that the tubing fluid temperature did not change much over long production times.

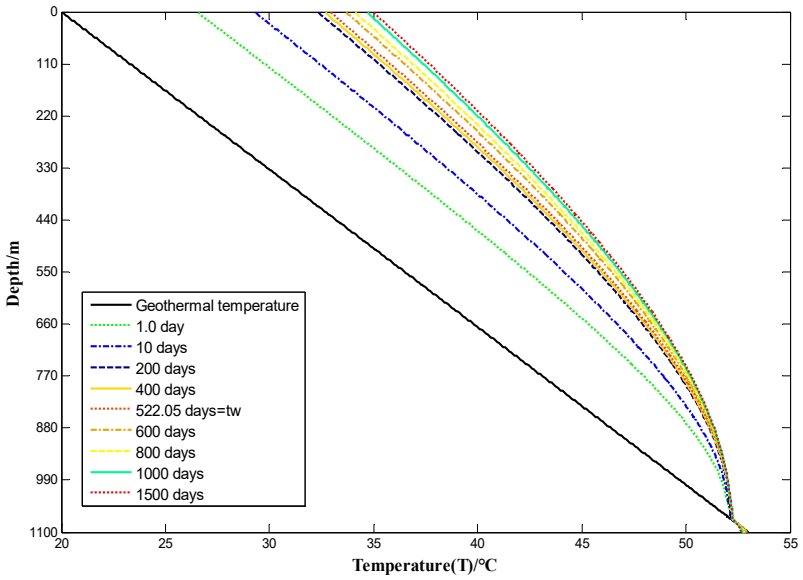


Figure 15. Fluid temperature in vertical tubing at the tubing-tubing wall interface (r = 0.04 m, 0 m ≤ z ≤ 1100 m) with different production time (t).

4.4.2. Sensitivity to Total Flow Rate of Wellhead (q_{rate})

The tubing fluid temperature distribution (r = 0.04 m, 0 m ≤ z ≤ 1100 m) with a different flow rate of the wellhead (q_{rate}) at different production times is shown in Figure 16. The results reveal that the wider the separation between the tubing fluid temperature and the initial (geothermal) temperature with high production rate. This is because the smaller flow rate of the wellhead, the smaller the upward seepage velocity of the tubing fluid is, and the more sufficient the fluid radial heat transfer will be, resulting in the heat transferred to the wellbore-formation interface from the wellbore fluid, therefore, becoming larger. Hence the greater the fluid flow velocity, the less heat is transferred in the radial direction and vice versa. Therefore, the larger the production rate, the higher the fluid temperature in the tubing.

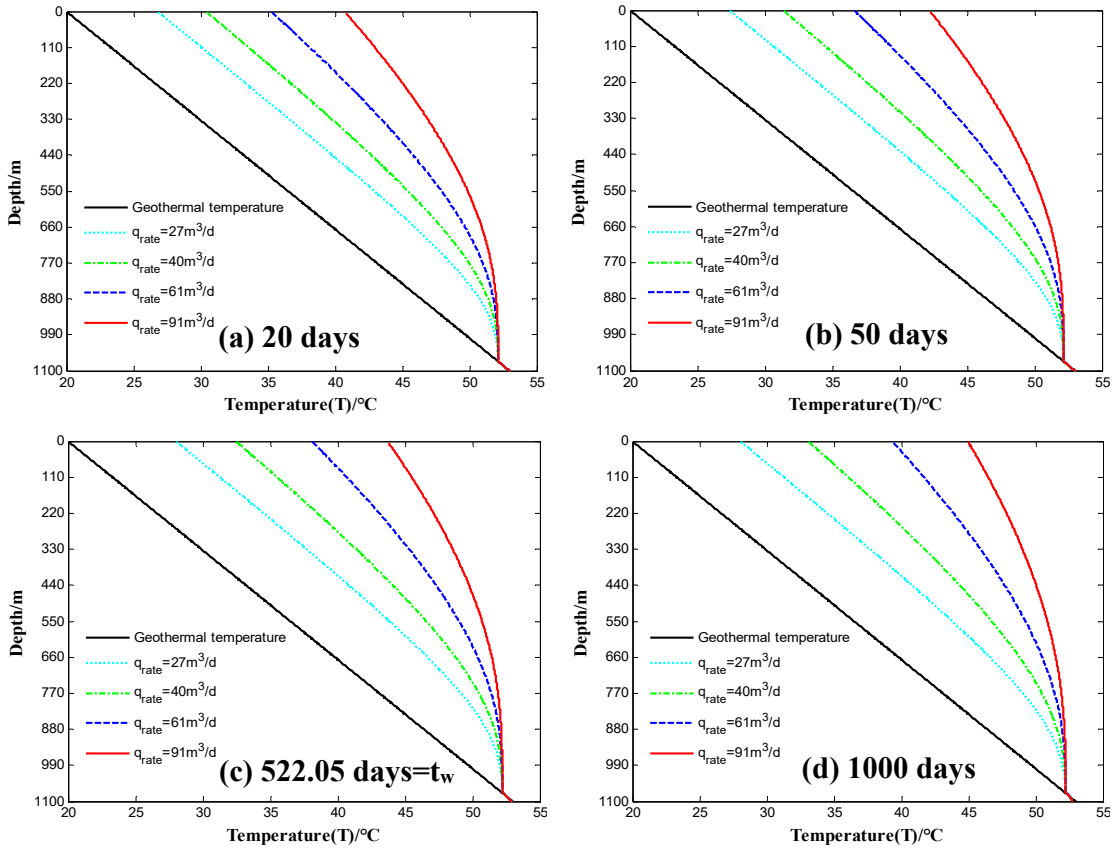


Figure 16. Fluid temperature in vertical tubing at the tubing-tubing wall interface (r = 0.04 m, 0 m ≤ z ≤ 1100 m) with a different flow rate of wellhead (q_{rate}). (**a**), (**b**), (**c**), (**d**) are the temperature profiles of 20, 50, 522.05, 1000 days of production time, respectively.

4.4.3. Sensitivity to TC of the Overburden

Figure 17 shows the overburden temperature variation at the wellbore-formation interface (r = 0.14 m, 0 m ≤ z ≤ 1000 m) with different TC. Materials with a high TC have excellent thermal conductivity, with the same heat flux and thickness, the temperature difference between the high-temperature side and the low-temperature side decreases with the increase of TC. As mentioned above, the overburden was heated by the high-temperature fluid in the tubing, thus with the increase of the TC, the overburden temperature was closer to the high-temperature fluid, in other words, it was hotter.

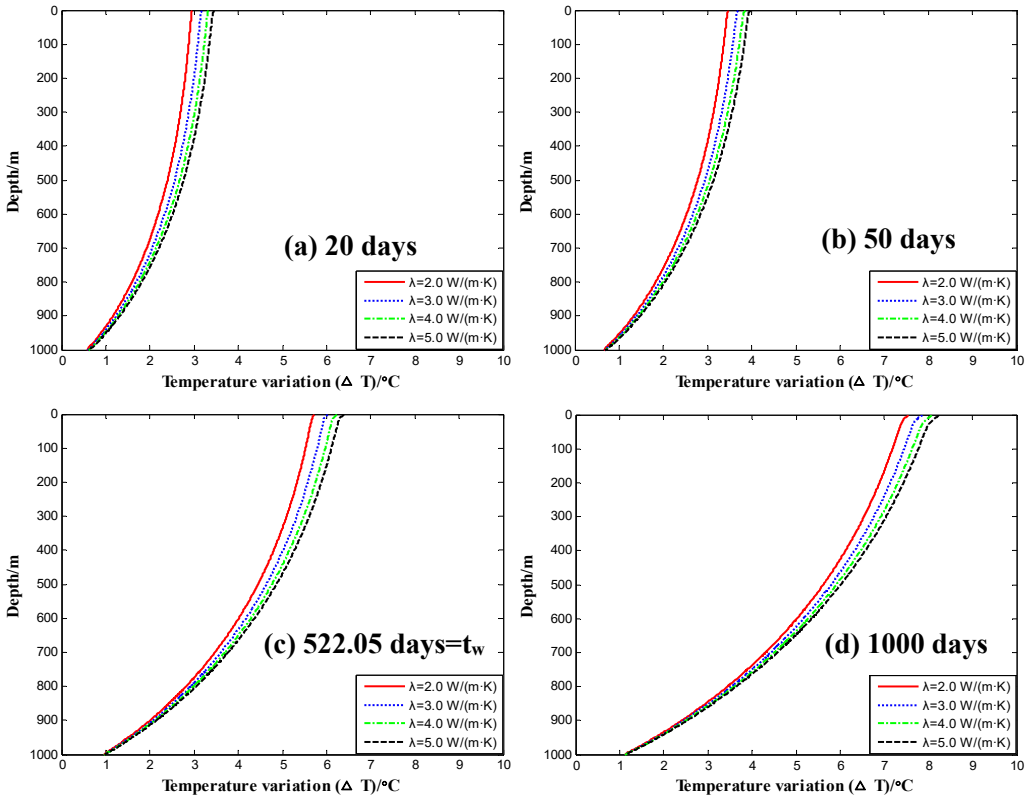


Figure 17. Overburden temperature variation at the wellbore-formation interface (r = 0.14 m, 0 m ≤ z ≤ 1000 m) with different thermal conductivity (TC). (**a**), (**b**), (**c**), (**d**) are the temperature profiles of 20, 50, 522.05, 1000 days of production time, respectively.

4.4.4. Sensitivity to VHC of Overburden

Figure 18 shows the overburden temperature variation at the wellbore-formation interface (r = 0.14 m, 0 m ≤ z ≤ 1000 m) with a different VHC. The smaller the VHC of the overburden, the smaller the absorbed heat for a 1 °C temperature rise. Hence, all things being equal, more heat can be left to continue to transfer to the overburden, which can make the temperature of the object point bigger. From another point of view, we know that the greater the thermal diffusivity ($\alpha = \lambda / \rho c$) is, the greater the ability of the system to even out the internal temperature, and the overburden can be heated by the high-temperature fluid in the tubing. Hence, with the decrease of the VHC (α will go up), the overburden temperature becomes closer to that of the high-temperature fluid. Thus, the overburden temperature will be higher.

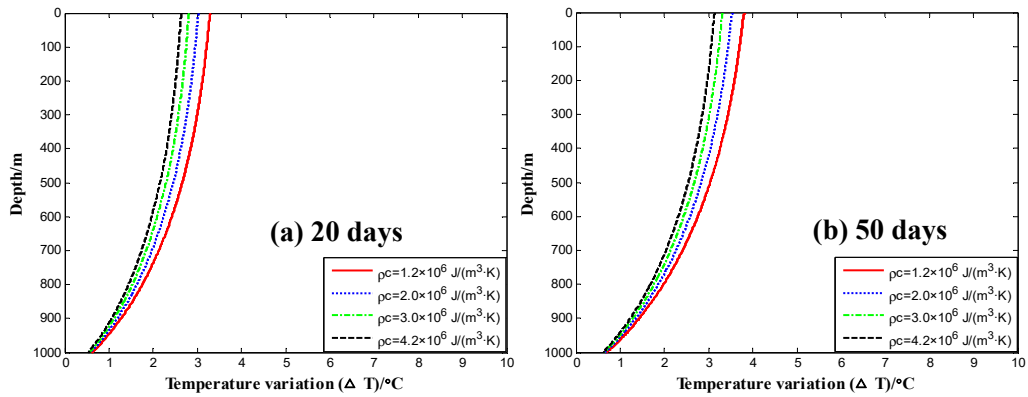


Figure 18. *Cont.*

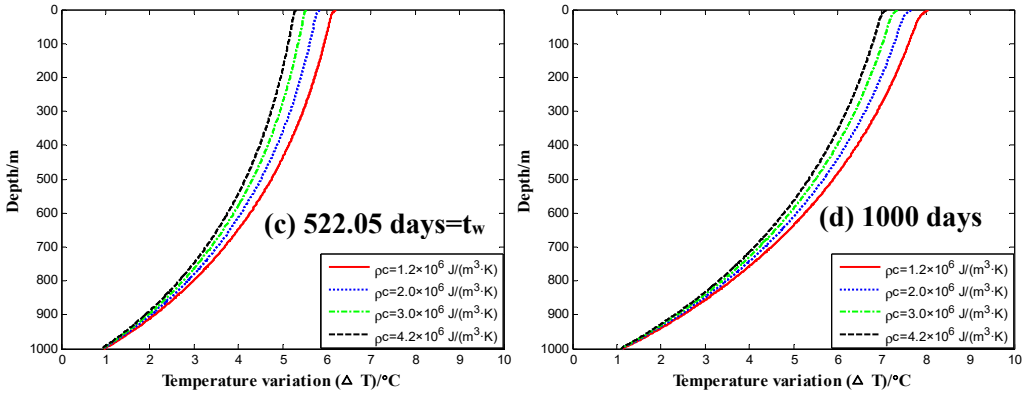


Figure 18. Overburden temperature variation at the wellbore-formation interface (r = 0.14 m, 0 m ≤ z ≤ 1000 m) with a different volumetric heat capacity (VHC). (**a**), (**b**), (**c**), (**d**) are the temperature profiles of 20, 50, 522.05, 1000 days of production time, respectively.

4.4.5. Sensitivity to Porosity (∅) of Pay Zones

The evolution of the formation temperature variation at the wellbore-formation interface (r = 0.14 m, 1000 m ≤ z ≤ 1100 m) with a different porosity (∅) during the 1500-day period is shown in Figure 19. We noticed that in the early stage of production ($t \leq t_w$ = 522.05 days, Figure 19a–f), the influence of porosity on the temperature profile first increases and then decreased but had little influence on the formation temperature in the later stages ($t > t_w$ = 522.05 days, Figure 19g–i).

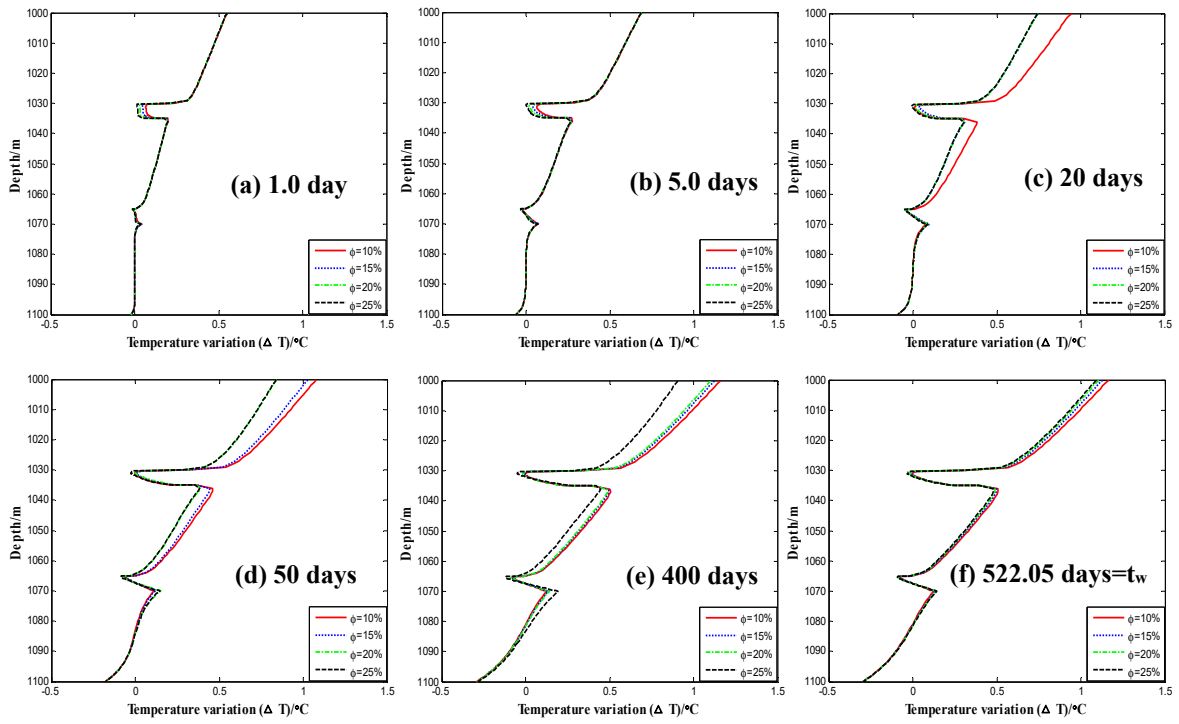


Figure 19. *Cont.*

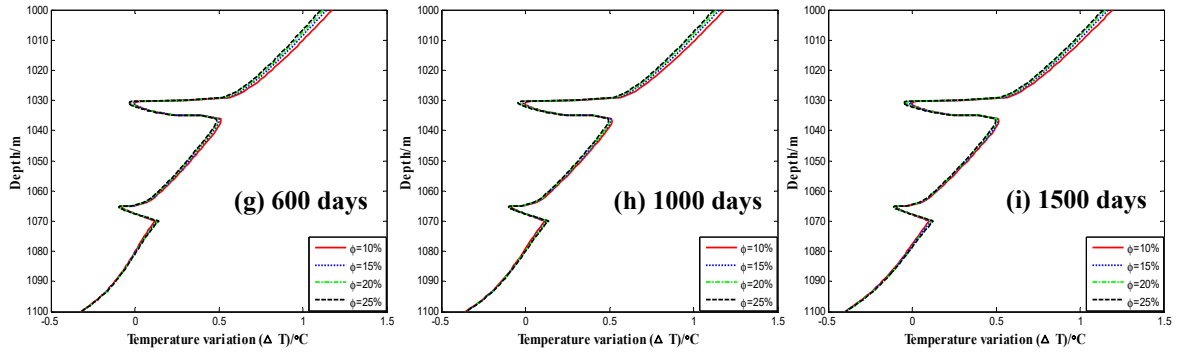


Figure 19. Formation temperature variation at the wellbore-formation interface (r = 0.14 m, 1000 m ≤ z ≤ 1100 m) with a different porosity (∅). (**a**–**i**) represent the temperature profiles from 1 day to 1500 days.

4.4.6. Sensitivity to Irreducible Water Saturation (s_{wi}) of Pay Zones

Figure 20 shows the formation temperature variation at the wellbore-formation interface (r = 0.14 m, 1000 m ≤ z ≤ 1100 m) with different irreducible water saturation (s_{wi}) for different production times. We can observe that the irreducible water saturation has an important impact on the formation temperature, which is because the variation of the initial irreducible water saturation greatly influenced the seepage parameters of pay zones (including the WBT, the "frontier" water saturation (s_{wf}) and the water content (f_w), etc.). Hence, the equivalent thermophysical parameters also changed greatly, arousing the temperature change significantly. In addition, the higher the irreducible water saturation, the bigger the temperature profile anomaly. We can also perceive that the influence degree of the irreducible water saturation on the formation temperature continuously increased at the beginning of production ($t < t_w$ = 522.05 days, Figure 20a–e)), while the impact on the temperature field decreased gradually in the later stages ($t \geq t_w$ = 522.05 days, Figure 20f–i). In addition, after reaching a stable state (Figure 20g–i), the variation of the irreducible water saturation (s_{wi}) had little effect on the temperature profile.

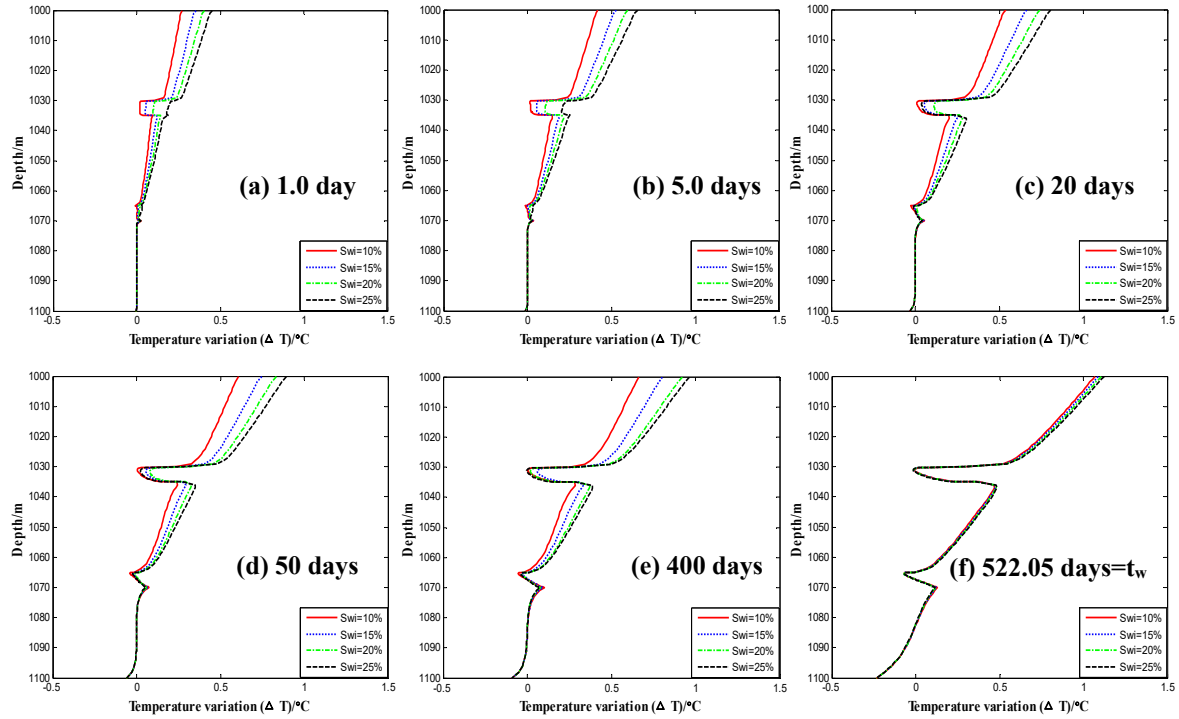


Figure 20. *Cont.*

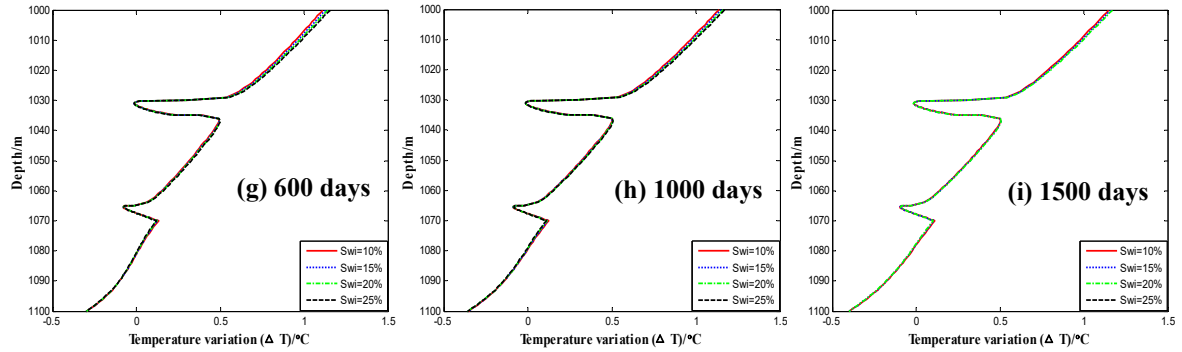


Figure 20. Formation temperature variation at the wellbore-formation interface (r = 0.14 m, 1000 m ≤z ≤ 1100 m) with different irreducible water saturations (s_{wi}). (**a**)–(**i**) represent the temperature profiles from 1 day to 1500 days.

5. Conclusions

(1) This study is applicable not only for single pay zone but also for multiple pay zones, which means we can treat the pay zone and surrounding earth as consisting of an arbitrary number of layers with different thermal and physical properties.

(2) Compared with analytical or semi-analytical models, our proposed model can calculate the whole well temperature distribution with considerably more actual conditions of heat exchange between wellbore and formation. As for other conventional numerical models, the seepage characteristics of the pay zones and the upward seepage velocity of the tubing fluid that change with depth were carefully investigated in the proposed coupled model. Thus, the interpreted temperature distributions were closer to the real temperature behavior of production well, which reduced the error in the temperature prediction.

(3) The novel method proposed in this study can be convenient to simulate the water saturation (s_w) and the WBT in the process of water flooding.

(4) The seepage effect from the pay zones to inside the tubing all had a great influence on the temperature field. Therefore, the saturation and seepage velocity of the two-phase fluid change with the production time should be highly valued. At the same time, the upward seepage velocity (v_z) of the fluid in tubing that changes with depth also cannot be neglected.

(5) As the fluids flow from the reservoir limit to the tubing, the temperature of pay zones decreased (the temperature change was negative). In addition, at any depth (z), the tubing fluid temperature change (1000 m ≤ z ≤ 1070 m) was close to the difference between the virgin fluid temperature (T_{sur} + 1070g_T) at the bottom of pay zone B and the initial geothermal temperature ($T_0 = T_{sur} + g_T z$) with a different depth.

(6) Pressure (P) of the pay zones was positively correlated with the production time for the water-flooding production well. In addition, the pressure drop was smaller near the reservoir limit and larger near the wellbore during the entire production life. Therefore, the radial seepage velocity (v_{wr} and v_{or}) of the reservoir fluid near the wellbore was greater than that far away from the wellbore.

(7) The sensitivity study indicated that the total production rate (q_{rate}) and the production time (t) had an essential effect on the tubing fluid temperature. The sensitivity of the porosity ($\emptyset$) and the irreducible water saturation (s_{wi}) to formation temperature was significantly different before and after the WBT. In addition, the overburden will be hotter with the lower VHC or the higher TC during the entire production life.

(8) In order to further improve the study, there are two main tasks for the next step. Firstly, based on the two-phase flow equation of immiscible oil–water, the 2-D water saturation and seepage velocity should be solved to match the 2-D coupled heat transfer model. Secondly, the fluids thermal properties (density, specific heat, thermal conductivity and dynamic viscosity) should be considered to vary with temperature.

Author Contributions: Conceptualization, H.M. and G.H.; Methodology, G.H. and H.M.; Software, G.H. and H.M.; Validation, G.H., H.M. and X.H.; Formal Analysis, G.H. and J.C.; Investigation, G.H., H.M., X.H. and J.C.; Resources, H.M. and X.H.; Data Curation, G.H.; Writing-Original Draft Preparation, G.H. and H.M.; Writing-Review & Editing, G.H., H.M. and J.C.; Visualization, J.L. and H.L.; Supervision, X.H., H.M. and H.P.; Project Administration, H.M.; Funding Acquisition, X.H. and H.M.

Funding: This research was funded by the financial support from the National Key Research and Development Program of China (2018YFC0604303, 2016YFC0600201, 2017YFC0602405), the National Nature Science Foundation of China (41630317).

Acknowledgments: The authors gratefully appreciate the financial support from the National Key Research and Development Program of China (2018YFC0604303, 2016YFC0600201, 2017YFC0602405), the National Nature Science Foundation of China (41630317). We also acknowledge the editors and reviewers for their constructive suggestions and comments.

Conflicts of Interest: The authors declare no conflicts of interest.

Nomenclature

c_o	specific heat capacity of oil, J/(kg K)
c_w	specific heat capacity of water, J/(kg K)
c_{s1}	specific heat capacity of porous media, J/(kg K)
c_{s2}	specific heat capacity of the matrix in pay zones, J/(kg K)
c_{pm}	heat capacity of wellbore fluid, J/(kg K)
c_r	ratio between the formation and the wellbore heat capacity, dimensionless
$f(t_D)$	the function of the dimensionless time (t_D)
f_o	oil content, dimensionless. $f_o = 1 - f_w$
f_w	water cut, dimensionless. Equation (2)
$f'_w(s_w)$	the derivative of water cut with respect to water saturation, dimensionless
$f_w(s_{w_array})$	water cut, the function of water saturation (s_{w_array}), dimensionless
$f'_w\left(s_{w_array}\right)$	the derivative of water cut ($f_w(s_{w_array})$) with respect to water saturation (s_{w_array}), dimensionless
$F'_{sw}(s_w(\ j\ ))$	the derivative of water cut with respect to water saturation for each grid node of the pay zone, dimensionless
g	acceleration due to gravity, m/s^2
g_c	conversion factor, 1.0 Kg·m/(s^2 ·N)
g_p	pressure gradient of formation, Mpa/m
g_T	geothermal gradient, °C/m
h	reservoir thickness/height, m
h_{over}	Thickness of the overburden
h_c	convection heat transfer coefficient, W/(m^2 K)
h_{to}	forced-convection heat transfer coefficient for the tubing fluid, W/(m^2 K)
h_{uc}	convective heat transfer coefficient for annulus fluid, W/(m^2 K)
h_{ur}	radiative heat transfer coefficient for the annulus, W/(m^2 K)
J	mechanical equivalent of heat, 1.0 N·m /J
K	absolute permeability of rock, μm^2
K_{ro}	relative permeability of oil phase, dimensionless. Equation (3)
K_{rw}	relative permeability of water phase, dimensionless. Equation (3)
k_{cas}	thermal conductivity of the casing material, W/(m K)
k_{cem}	thermal conductivity of the cement, W/(m K)
k_e	thermal conductivity of the earth (formation), W/(m K)
k_t	thermal conductivity of the tubing material, W/(m K)
N_{uf}	Nusselt number, dimensionless
P_{ref}	reference pressure at a specific location, Mpa
P	pressure of the two-phase system in pay zones, Mpa
P_A	The ratio of the flow rate of pay zone A to the total flow rate of wellhead (q_{rate}), %
P_B	The ratio of the flow rate of pay zone B to the total flow rate of wellhead (q_{rate}), %
P_{rf}	Prandtl number, dimensionless

q_o	oil flow rate, m^3/s
q_{rate}	total flow rate, m^3/s
q_w	water flow rate, m^3/s
r	the radial distance from borehole axis, m
r_{ci}	inside radius of the casing, m
r_{co}	outside radius of the casing, m
r_e	the radial distance between the borehole axis and reservoir limit, m
r_i	the radial distance between discrete nodes and borehole axis, m
r_{ti}	inside radius of tubing, m
r_{to}	outside radius of tubing, m
r_{wb}	outside radius of wellbore, m
r_{ab}	outside radius of the cement A, m
r_{bb}	outside radius of the cement B, m
r_{cb}	outside radius of the cement C, m
r_{wf}	the radial distance between the borehole axis and water drive front at different production time, m
R_{ef}	Reynolds number, dimensionless
R_{error}	relative error of the temperatures, dimensionless
s_o	oil saturation, dimensionless. $s_o = 1 - s_w$.
s_w	water saturation, dimensionless. The calculation process is shown in Figure 6.
$s_w(j)$	water saturation of each grid node in reservoir profile grid model
s_{w_array}	a set of water saturation from s_{wi} to 100% with linear interpolation by setting water saturation step Δs, dimensionless
s_{wf}	frontier water saturation for water drive oil in pay zones, dimensionless
s_{wi}	irreducible water saturation in pay zones, dimensionless
s_{fi}	initial water saturation of porous media, dimensionless
t	production time, day
t_D	diffusion time function, dimensionless
T	temperature at a specific production time, °C
T_0	initial (undisturbed) temperature at any given depth, °C
T_{sur}	initial surface temperature
T_{analy}	temperature calculated by Hasan analytical solution, °C
T_{bl}	temperature of pay zones at interfaces between the pay zone and the adjacent formation, °C
T_{bs}	temperature of adjacent formations at interfaces between the pay zone and the adjacent formation, °C
T_{ei}	undisturbed formation temperature at any given depth, °C
T_f	wellbore (tubing) fluid temperature, °C
T_{l1}	fluid temperature at the tubing/ tubing wall interface, °C
T_{l2}	fluid temperature of the tubing at the interface between the tubing and pay zone, °C
T_{num}	temperature obtained by a numerical method, °C
T_{s1}	temperature of tubing wall at the tubing/ tubing wall interface, °C
T_{s2}	temperature of the pay zone at the interface between the tubing and the pay zone, °C
T_{Wb}	wellbore/earth interface temperature, °C
t_w	water breakthrough time for tubing, day
U_{to}	overall heat transfer coefficient, $W/(m^2\ K)$
v_o	seepage velocity of the oil phase, m/s
v_{or}	radial seepage velocity of the oil phase in pay zones, m/s. Equation (7)
v_w	seepage velocity of the water phase, m/s
v_{wr}	radial seepage velocity of the water phase in pay zones, m/s. Equation (7)
v_z	upward seepage velocity of the fluid in the tubing, m/s. Equation (21)
w	total mass flow rate, kg/s
x	the radial distance from the borehole axis in rectangular coordinates
z	variable well depth from surface, m
z_b	the boundaries between the pay zones and the adjacent formations, m
z_{bh}	total well depth from surface, m

z_{max}	total well depth from surface, m
α_{ft}	thermal diffusivity of the formation, m^2/s
θ	pipe inclination angle from horizontal, degrees
λ_f	thermal conductivity of fluid, W/(m K)
λ_l	equivalent thermal conductivity of the fluid in the tubing, W/(m K)
λ_o	thermal conductivity of the oil phase, W/(m K)
λ_w	thermal conductivity of the water phase, W/(m K)
λ_{s1}	thermal conductivity of porous media, W/(m K)
λ_{s2}	thermal conductivity of matrix in pay zones, W/(m K)
λ^*_{s2}	equivalent thermal conductivity of pay zones, W/(m K)
λ^*_{s1}	equivalent thermal conductivity of porous media, W/(m K)
μ	fluid dynamic viscosity, Pa·s
μ_o	dynamic viscosity of the oil phase, Pa·s
μ_w	dynamic viscosity of the water phase, Pa·s
ρ_o	the density of oil, kg/m^3
ρ_w	the density of water, kg/m^3
ρ_{s1}	the density of porous media, kg/m^3
ρ_{s2}	the density of matrix in pay zones, kg/m^3
$(\rho c)_l$	equivalent volumetric heat capacity of fluid in the tubing, $(J/(m^3 \cdot K))$
$(\rho c)^*_{s1}$	equivalent volumetric heat capacity of porous media, $(J/(m^3 \cdot K))$
$(\rho c)^*_{s2}$	equivalent volumetric heat capacity of pay zones, $(J/(m^3 \cdot K))$
φ	parameter combining the Joule-Thompson and kinetic energy effects
$\emptyset$	porosity, dimensionless
$\emptyset_1$	porosity of porous media, dimensionless
$\emptyset_2$	porosity of pay zones, dimensionless
Δs_w	water saturation step, dimensionless
$\Delta T = T - T_0$	where T represents the downhole temperature at a specific production time and T_0 is the initial (undisturbed) downhole temperature, °C
Δt	the time interval of the production time, day
Δx	the radial discrete spacing, m
Δz	the longitudinal discrete spacing, m

Appendix A

In this model, the finite difference discrete scheme can be divided into two parts: (1) in the longitudinal direction, the grid with equal spacing was adopted; (2) in the radial direction, the uniform spacing grid was used in the wellbore (from the borehole axis to outside radius of the cement C), while the formation grid was treated with logarithmic method. The grid mesh generation is shown in Figure A1, that is, the grid with equal spacing was used in the range of 0–N and 0–M_{wb}, while the grid with equal logarithmic spacing was used from M_{wb} to M.

In order to simplify the form of the difference equation in this study, the equations can be transformed from the r-z coordinate system to the x-z coordinate system. According to the coordinate transformation principle, the treatments of the wellbore-formation grids can be classified into the following two methods:

(1) The uniform spacing grid was used in wellbore, and the grid subdivision can be conducted according to the following formula:

$$\Delta x = \frac{r_e - r_{cb}}{N} \tag{A1}$$

Radial grid nodes in the wellbore can be expressed as:

$$r_j = j\Delta x = x_j \tag{A2}$$

The radial differential expression in the wellbore can be derived from Equation (A2):

$$dr = dx. \tag{A3}$$

(2) The formation grid was treated with logarithmic method, and the grid partition formula can be constructed as:

$$\Delta x' = \frac{ln(r_e) - ln(r_{cb})}{N} \tag{A4}$$

The location of formation radial mesh nodes can be deduced:

$$r_j = r_{cb} \cdot e^{j\Delta x'} = r_{cb} \cdot e^{x_j'} \tag{A5}$$

Hence, the radial differential expression of the formation can be derived from Equation (A5):

$$dr = rdx \tag{A6}$$

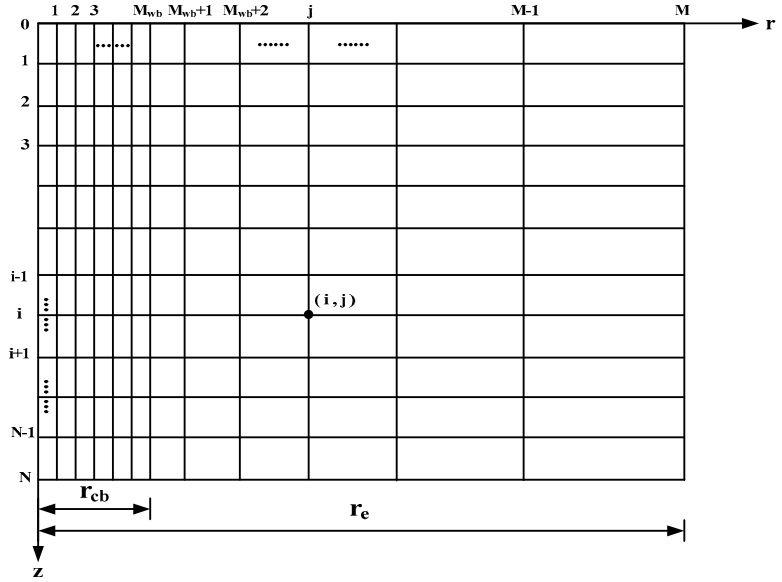


Figure A1. schematic of the downhole mesh generation.

Appendix B

In the calculation of the pressure field of the pay zones, the pressure was calculated by recursive algorithm from the supply edge to the inside radius of the wellbore, hence the discrete form of Equation (16) can be described as:

$$\Lambda_{i+1,j}\left(P_{i+1,j}^{n+1} - P_{i,j}^{n+1}\right) = -\frac{Q\Delta x}{2\pi h} \tag{A7}$$

where

$$\Lambda_{i+1,j} = (\Lambda_w)_{i+1,j} + (\Lambda_o)_{i+1,j} = (kk_{rw}/\mu_w)_{i+1,j} + (kk_{ro}/\mu_o)_{i+1,j}. \tag{A8}$$

In this model, the five-point implicit difference method was used to solve the downhole temperature field. Hence their finite difference discrete schemes are described as follows:

(1) The heat-transfer finite difference equation in the tubing can be written as:

$$\begin{gathered}(a_1 - a_{2i})T_{i-1,j}^{m+1} + (a_4 - 2a_1 - 2a_3 - a_5)T_{i,j}^{m+1} + (a_1 + a_{2i})T_{i+1,j}^{m+1} + a_3T_{i,j-1}^{m+1} + \\ (a_3 - a_4)T_{i,j+1}^{m+1} = -a_5T_{i,j}^{m}\end{gathered} \tag{A9}$$

where

$$a_1 = \frac{\lambda_l}{(\Delta x)^2}, a_{2i} = \frac{\lambda_l}{2r_i\Delta x}, \; a_3 = \frac{\lambda_l}{(\Delta z)^2}, \; a_4 = \frac{(\rho c)_l v_z}{\Delta z}, \; a_5 = \frac{(\rho c)_l}{\Delta t}. \tag{A10}$$

(2) The transient temperature field finite difference equation for the tubing wall, tubing-casing annulus, casing, cement, overburden and surrounding formations can be given by:

$$b_{1i}T_{i-1,j}^{m+1} + (-2b_{1i} - 2b_2 - b_3)T_{i,j}^{m+1} + b_{1i}T_{i+1,j}^{m+1} + b_2T_{i,j-1}^{m+1} + b_2T_{i,j+1}^{m+1} = -b_3T_{i,j}^{m} \tag{A11}$$

where

$$b_{1i} = \frac{\lambda_{s1}^*}{r_i^2(\Delta x)^2}, b_2 = \frac{\lambda_{s1}^*}{(\Delta z)^2}, b_3 = \frac{(\rho c)_{s1}^*}{\Delta t}. \tag{A12}$$

(3) We can express the temperature field finite difference equation of the pay zones as:

$$c_{1i}T_{i-1,j}^{m+1} + (c_{3i} - 2c_{1i} - 2c_2 - c_4)T_{i,j}^{m+1} + (c_{1i} - c_{3i})T_{i+1,j}^{m+1} + c_2T_{i,j-1}^{m+1} + c_2T_{i,j+1}^{m+1} = -c_4T_{i,j}^{m} \tag{A13}$$

where

$$c_{1i} = \frac{\lambda_{s2}^*}{r_i^2(\Delta x)^2},\ c_2 = \frac{\lambda_{s2}^*}{(\Delta z)^2},\ c_{3i} = \frac{(\rho cv)_r}{r_i\Delta x},\ c_4 = \frac{(\rho c)_{s2}^*}{\Delta t}. \tag{A14}$$

Appendix C

A five-point implicit finite difference equation can be written as:

$$a_{i,j}^* u_{i-1,j}^{n+1} + b_{i,j}^* u_{i,j}^{n+1} + c_{i,j}^* u_{i+1,j}^{n+1} + d_{i,j}^* u_{i,j-1}^{n+1} + e_{i,j}^* u_{i,j+1}^{n+1} = f_{i,j}^*. \tag{A15}$$

We can convert Equation (A15) into a block triangular matrix, where AX = F [39]:

$$\begin{bmatrix} C_1 & D_2 & & & 0 \\ B_1 & C_2 & D_3 & & \\ & B_2 & C_3 & \ddots & \\ & \ddots & \ddots & & D_N \\ 0 & & & B_{N-1} & C_{N-1} \end{bmatrix} \begin{bmatrix} X_1 \\ X_2 \\ \vdots \\ X_{N-1} \\ X_N \end{bmatrix} = \begin{bmatrix} F_1 \\ F_2 \\ \vdots \\ F_{N-1} \\ F_N \end{bmatrix} \tag{A16}$$

where

$$X = \left[\overbrace{\overbrace{u_{1,1}, u_{2,1}, u_{3,1}, \cdots u_{M,1}}^{M}, \overbrace{u_{1,2}, u_{2,2}, u_{3,2}, \cdots u_{M,2}}^{M}, \cdots, \overbrace{u_{1,N}, u_{2,N}, u_{3,N}, \cdots u_{M,N}}^{M}}^{N\times M} \right]^T. \tag{A17}$$

In Equation (A16), $B_i(i = 1,2,3, \ldots, N-1)$, $C_i(i = 1,2,3, \ldots, N-1)$ and $D_i(i = 2,3, \ldots, N)$ are $M \times M$ block matrix, $X_i(i = 1,2,3 \ldots N)$ and $F_i(i = 1,2,3 \ldots N)$ are $M \times 1$ block matrix. In addition, matrix A can be decomposed into the following special lower triangular matrix (L) and upper triangular matrix (U) [40]:

$$= \begin{bmatrix} H_1 & & & & 0 \\ G_1 & H_2 & & & \\ & \ddots & \ddots & & \\ & & G_{N-2} & H_{N-1} & \\ 0 & & & G_{N-1} & H_N \end{bmatrix} U = \begin{bmatrix} I_1 & J_2 & & & 0 \\ & I_2 & J_3 & & \\ & & \ddots & \ddots & \\ & & & I_{N-1} & J_N \\ 0 & & & & I_N \end{bmatrix}. \tag{A18}$$

In Equation (A18), $G_i(i = 1,2,3, \ldots, N-1)$, $H_i(i = 1,2,3, \ldots, N)$ and $J_i(i = 1,2,3, \ldots, N)$ are $M \times M$ block matrix,$I_i(i = 1,2,3, \ldots, N)$ is $M \times 1$ unit matrix. In addition, LU = A.

The undetermined coefficient method can be used to solve the non-zero elements in L and U. Hence we can combine Equations (A16) and (A18) to yield all non-zero elements in matrixes L and U:

$$G_{i-1} = B_{i-1}, \qquad i = 2,3,\cdots N \tag{A19}$$

$$H_i = \begin{cases} C_i, & i = 1 \\ C_i - G_{i-1} \times J_i, & i = 2,3,\cdots N \end{cases} \tag{A20}$$

$$J_{i+1} = H_i^{-1} \times D_{i+1}, \qquad i = 1,2,3,\cdots N-1. \tag{A21}$$

If we assume UX = Z, we can write LUX = F as LZ = F. Then, we can derive the expression for Z:

$$\begin{cases} Z_1 = H_1^{-1} \times F_1 = C_1^{-1} \times F_1 \\ Z_i = H_i^{-1} \times (F_i - G_{i-1} \times Z_{i-1}) \\ \quad = H_i^{-1} \times (F_i - B_{i-1} \times Z_{i-1}), i = 2,3,\cdots N \end{cases} \tag{A22}$$

Then we can combine Equations (A18), (A21) and UX = Z to yield the expression for X:

$$\begin{cases} X_N = Z_N \\ X_i = Z_i - J_{i+1} \times X_{i+1}, \ \ i = N-1, N-2, \cdots 1 \end{cases} . \tag{A23}$$

The process of solving Z_i (i = 1, 2, . . . , N) in Equation (A22) and X_i (i = N, N–1, ⋯, 1) in Equation (A23) is called the chasing method. In addition, this kind of algorithm was used to solve the block tridiagonal systems in this study.

References

1. Kaiser, M.J. Modeling the time and cost to drill an offshore well. *Energy* **2009**, *34*, 1097–1112. [CrossRef]
2. Nian, Y.L.; Cheng, W.L. Evaluation of geothermal heating from abandoned oil wells. *Energy* **2018**, *142*, 592–607. [CrossRef]
3. Lyu, Z.H.; Song, X.Z.; Li, G.S. Numerical analysis of the downhole flow field with compressible fluid in hydrothermal jet drilling. *Int. J. Therm. Sci.* **2018**, *132*, 322–334. [CrossRef]
4. Yu, B.; Sun, S.Y.; Wei, J.J.; Sun, Y.W.; Cai, W.H. Numerical simulation of fluid flow and heat transfer processes 2014. *Adv. Mech. Eng.* **2015**, *7*, 645351. [CrossRef]
5. Jin, N.D.; Nie, X.B.; Yin, Z.; Zhao, F.H. Investigation on the applicability of oil/water two-phase profiles interpretation based on temperature and flowmeter logs. In Proceedings of the 2003 International Conference on Machine Learning and Cybernetics, Xi'an, China, 5 November 2003.
6. Ferreira, M.V.D.; Hafemann, T.E.; Barbosa, J.R.; Sliva, A.K.; Hasan, R. A numerical study on the thermal behavior of wellbores. *SPE Prod. Oper.* **2016**, *32*, 564–574. [CrossRef]
7. Lauwerier, H.A. The transport of heat in an oil layer caused by the injection of hot fluid. *Appl. Sci. Res. Sect.* **1955**, *5*, 145–150. [CrossRef]
8. Lesem, L.B.; Greytok, F.; Marotta, F.; Mcketta, J.J., Jr. A method of calculating the distribution of temperature in flowing gas wells. *Petroleum Trans. AIME* **1957**, *210*, 169–176.
9. Ramey, H.J. Wellbore heat transmission. *J. Pet. Technol.* **1962**, *14*, 427–435. [CrossRef]
10. Satter, A. A prediction method for conduction heating of reservoirs by steam injection. In Proceedings of the Fall Meeting of the Society of Petroleum Engineers of AIME, New Orleans, LA, USA, 1–4 October 1967; SPE 1950, pp. 1–12. [CrossRef]
11. Raymond, L.R. Temperature distribution in a circulating drilling fluid. *J. Pet. Technol.* **1969**, *21*, 333–341. [CrossRef]
12. Marshall, D.W.; Bentsen, R.G. A computer model to determine the temperature distributions in a wellbore. *J. Can. Pet. Technol.* **1982**, *21*, 63–75. [CrossRef]
13. Kabir, C.S.; Hasan, A.R.; Jordan, D.L.; Wang, X.W. A wellbore/reservoir simulator for testing gas wells in high-temperature reservoirs. *SPE Form. Eval.* **1996**, *11*, 128–134. [CrossRef]
14. Hasan, A.R.; Kabir, C.S.; Wang, X.W. Development and application of a wellbore/reservoir simulator for testing oil wells. *SPE Form. Eval.* **1997**, *12*, 182–188. [CrossRef]
15. Hasan, A.R.; Kabir, C.S.; Wang, X.W. Wellbore two-phase flow and heat transfer during transient testing. *SPE J.* **1998**, *3*, 174–180. [CrossRef]
16. Izgec, B.; Kabir, C.S.; Zhu, D. Transient fluid and heat flow modeling in coupled wellbore/ reservoir systems. *SPE Reserv. Eval. Eng.* **2007**, *10*, 294–301. [CrossRef]
17. Wu, B.S.; Liu, T.L.; Zhang, X.; Wu, B.L.; Jeffrey, R.G.; Bunger, A.P. A transient analytical model for predicting wellbore/reservoir temperature and stresses during drilling with fluid circulation. *Energies* **2018**, *11*, 42. [CrossRef]
18. Farshad, F.F.; Garber, J.D.; Lorde, J.N. Predicting temperature profiles in producing oil wells using artificial neural networks. *Eng. Comput.* **2000**, *17*, 735–754. [CrossRef]
19. Lee, T.C.; Duchkov, A.D.; Morozov, S.G. Determination of thermal properties and formation temperature from borehole thermal recovery data. *Geophysics* **2003**, *68*, 1835–1846. [CrossRef]
20. Romero-Juarez, A. A note on the theory of temperature logging. *SPE J.* **1969**, *9*, 375. [CrossRef]
21. Curtis, M.R.; Witterholt, E.J. Use of the temperature log for determining flow rates in producing wells. In Proceedings of the Fall Meeting of the Society of Petroleum Engineers of AIME, Las Vegas, NV, USA, 30 September–3 October 1973; SPE 4637, pp. 1–12. [CrossRef]

22. Smith, R.C.; Steffens, R.J. Computer study of factors affecting temperature profiles in water injection wells. *J. Pet. Technol.* **1970**, *22*, 1447–1458. [CrossRef]
23. Ganguly, S. Exact Solution of Heat Transport Equation for a Heterogeneous Geothermal Reservoir. *Energies* **2018**, *11*, 2935. [CrossRef]
24. Shi, Y.; Song, Y.J.; Liu, H. Numerical simulation of downhole temperature distribution in producing oil wells. *Appl. Geophys.* **2008**, *5*, 340–349. [CrossRef]
25. Mostofinia, M.; Mohammadi, M.; Pourafshary, P. A coupled wellbore/reservoir simulator to model temperature distribution and inflow rate profile in wells with multiple pay zones. *Pet. Sci. Technol.* **2012**, *30*, 575–584. [CrossRef]
26. Shang, W.; Sarica, C. Temperature Prediction for Two-Phase Oil/Water Stratified Flow. In Proceedings of the 7th North American Conference on Multiphase Technology, Banff, AB, Canada, 2–4 June 2010.
27. Hasan, A.R.; Kabir, C.S. Wellbore heat-transfer modeling and applications. *J. Pet. Sci. Eng.* **2012**, *86*, 127–136. [CrossRef]
28. Mao, Y.L.; Zeidouni, M. Temperature transient analysis for bounded oil reservoir under depletion drive. *Int. J. Therm. Sci.* **2018**, *130*, 457–470. [CrossRef]
29. Shen, P.P. *Flow and Transport of Oil and Water in Porous Media*; Petroleum Industry Publishing House: Beijing China, 2000.
30. Hill, A.D. Production logging: Theoretical and interpretive Elements. In *Monograph Series*; SPE: Richardson, TX, USA, 1990; ISBN 978-1-55563-030-0.
31. Huang, R.; Wu, X.D.; Wang, R.H.; Li, H. An estimation method of Water drive displacement based on formation permeability distribution and inverse problem modeling. *Adv. Mech. Eng.* **2014**, *5*, 409657. [CrossRef]
32. Parker, J.C.; Lenhard, R.J.; Kuppusamy, T. A parametric model for constitutive properties governing multiphase flow in porous media. *Water Resour. Res.* **1987**, *23*, 618–624. [CrossRef]
33. Wang, S.R.; Cheng, L.S.; Xue, Y.C.; Huang, S.J.; Wu, Y.H.; Jia, P.; Sun, Z. A semi-analytical method for simulating two-phase flow performance of horizontal volatile oil wells in fractured carbonate reservoirs. *Energies* **2018**, *11*, 2700. [CrossRef]
34. Fagley, J.; Fogler, H.S.; Davenport, C.B. An improved simulation for interpreting temperature logs in water injection well. *Soc. Pet. Eng. J.* **1982**, *22*, 709–718. [CrossRef]
35. Hasan, A.R.; Kabir, C.S. Aspects of wellbore heat transfer during two-phase flow. *SPE Prod. Facil.* **1994**, *9*, 211–216. [CrossRef]
36. Hasan, A.R.; Kabir, C.S. Heat transfer during two-phase flow in wellbores: Part I—Formation temperature. In Proceedings of the SPE Annual Technical Conference and Exhibition, Dallas, TX, USA, 6–9 October 1991; SPE 22866, pp. 469–478. [CrossRef]
37. Willhite, G.P. Over-all heat transfer coefficients in steam and hot water injection wells. *J. Pet. Technol.* **1967**, *19*, 607–615. [CrossRef]
38. Cheng, W.L.; Huang, Y.H.; Lu, D.T.; Yin, H.R. A novel analytical transient heat-conduction time function for heat transfer in steam injection wells considering the wellbore heat capacity. *Energy* **2011**, *36*, 4080–4088. [CrossRef]
39. Koulaei, M.H.; Toutounian, F. Factored sparse approximate inverse of block tridiagonal and block pentadiagonal matricies. *Appl. Math. Comput.* **2007**, *18*, 223–234. [CrossRef]
40. Wu, C.Y. Stability of block LU factorization for block tridiagonal block H-matrices. *J. Comput. Appl. Math.* **2012**, *236*, 2673–2684. [CrossRef]



© 2019 by the authors. Licensee MDPI, Basel, Switzerland. This article is an open access article distributed under the terms and conditions of the Creative Commons Attribution (CC BY) license (http://creativecommons.org/licenses/by/4.0/).